Dimensionality and Fermi Surface of Low-Dimensional Metals†

Enric Canadell

Institut de Ciència de Materials de Barcelona (CSIC), Campus de la U.A.B., 08193 Bellaterra, Spain

Received March 23, 1998. Revised Manuscript Received June 11, 1998

Low-dimensional metals exhibit a wealth of interesting phenomena associated with the special topology of their Fermi surfaces. These Fermi surfaces contain a very rich information concerning not only the dimensionality of the conductivity but also the possibility of different metal-to-insulator or metal-to-metal transitions. Because the shape of the Fermi surface is to a great extent imposed by the crystal structure, it is important to develop conceptual models to find the link between the crystal structure and the Fermi surface of these systems. An approach based on simple ideas of overlap, symmetry, and chemical bonding is used to analyze some puzzling observations concerning a number of low-dimensional metals including oxides, bronzes, and molecular metals.

Contents

Low-dimensional metals have certainly led to one of the more interesting and fruitful chapters in modern solid-state science. The interest on these materials finds its roots in the theoretical developments by Peierls[1] and Fröhlich[2] more than 40 years ago. However, it was the seminal work by Wilson, DiSalvo, and Mahajan[3] and by Williams[4] on transition-metal dichalcogenides, as well as the almost simultaneous reports on the preparation of the first truly organic molecular metal, TTF-TCNQ (TTF: tetrathiafulvalene, TCNQ: tetracyanoquinodimethane),[5,6] which launched an enormous effort on the study of these materials. The discovery of nonlinear conductivity in $NbSe_3$[7] and the stabilization of superconductivity under pressure in quasi-one-dimensional $(TMTSF)_2PF_6$,[8] were major events in the development of the physics and chemistry of low-dimensional materials. Over the years, this research field has grown tremendously both in terms of new physical phenomena (high T_c superconductivity, field-induced spin density waves, etc.) and new materials that have been discovered (or rediscovered) as low-dimensional conductors (molybdenum oxides and bronzes, transition metal chalcogenides, a host of new molecular conductors, etc.).[9]

Many of the interesting properties of low-dimensional metals are related to the special topology of their Fermi surface which, in the end, is imposed by the crystal structure. Thus, to discuss the origin of these properties, and more importantly, if we want to have some control over them, it is important to be able to understand how the shape of the Fermi surface is related to the crystal structure. For instance, this understanding is very important for low-dimensional molecular conductors. In that case, there are many examples showing that very slight modifications in the crystal structure can drastically change the conducting properties. As will be discussed later, a detailed knowledge of the correlation between the crystal and electronic structure (and thus, the Fermi surface) can be very helpful in tuning the transport properties of molecular conductors.

Another important issue in this field is that of the meaning of the dimensionality concept. Quite frequently it is used in a structural sense. However, there is no reason why a solid with a given structural dimensionality could not exhibit transport and/or other physical properties indicating a lower dimensionality. For instance, the crystal structure of the blue bronze $K_{0.3}MoO_3$ is made up of $MoO_3^{0.3-}$ layers between which reside the K^+ cations. Thus, from a structural viewpoint, it is a typical two-dimensional (2D) solid. However, in terms of the conductivity it is a pseudo-one-dimensional (pseudo-1D) metal. The purple bronze KMo_6O_{17} is a 2D system both in terms of structure and electrical conductivity. Nevertheless, at low tempera-

† Dedicated to the memory of Jeremy K. Burdett and Jean Rouxel.

10.1021/cm980176o CCC: $15.00
Published on Web 08/22/1998

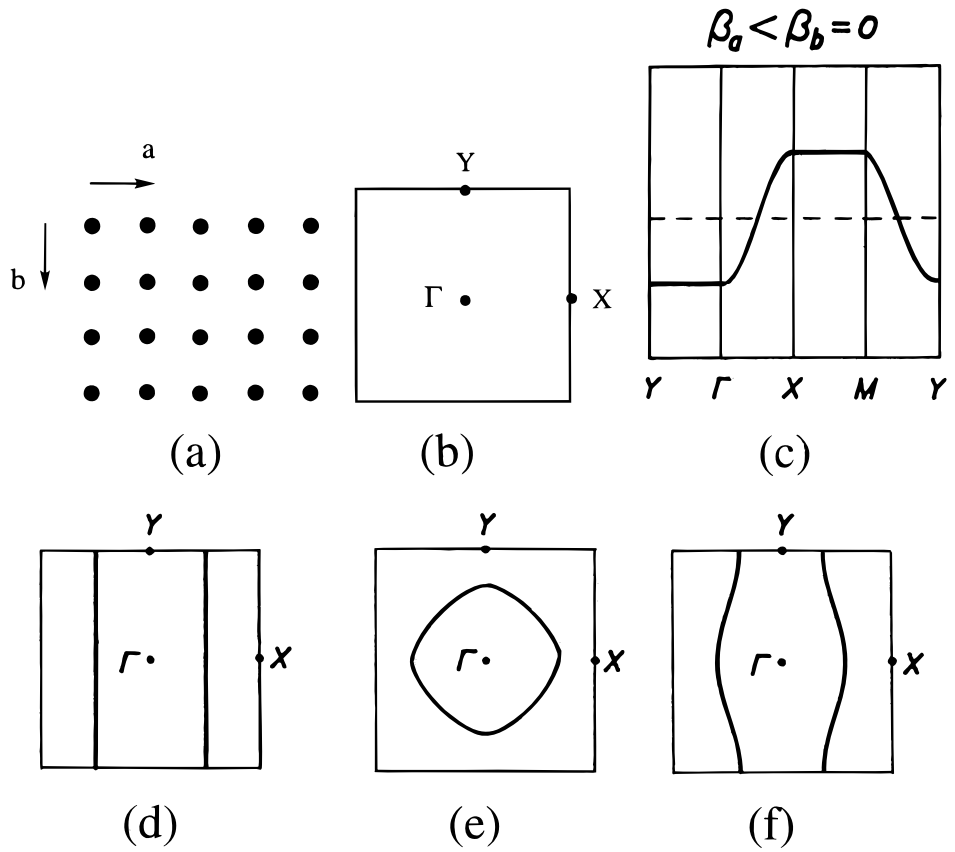

Figure 1. Schematic representation of (a) a rectangular lattice, (b) its first Brillouin zone, and (c) the band structure when $\beta_a \neq 0$ and $\beta_b = 0$. Three different Fermi surfaces typical of 1D, 2D, and pseudo-1D metals are shown in d, e, and f, respectively.

ture, it exhibits a structural modulation as if it was a 1D system. Again, it is clear that understanding the relationship between the crystal and electronic structures is a fundamental step in the study of low-dimensional materials.

As mentioned, the interest of low-dimensional metals stems to a great extent from the special topology of their Fermi surfaces. There is a wealth of information contained in the Fermi surface of a metallic system when appropriately decoded, not only concerning the dimensionality of the conductivity but also about the possibility of different metal-to-insulator or metal-to-metal transitions related to the stabilization of charge or spin density waves, etc. Of course, the shape of the Fermi surface is to a great extent imposed by the crystal structure. There are, however, some subtleties to be taken into account in relating the crystal and electronic structures.[10] The main object of this review is to show, with the help of some selected examples, that to find the link between the crystal structure and the Fermi surface of low-dimensional metals is quite often a very simple task once the crystal structure of the system is carefully considered.

Electronic Structure of Metals: Basic Concepts

The electronic structure of low-dimensional metals is usually discussed in terms of band theory.[10] To briefly introduce the basic terminology[11] we will use in our discussion, let us consider a rectangular 2D lattice with repeat vectors a and b, as shown in Figure 1a. Each lattice site may be assumed to have one orbital and one electron. Under the approximation of nearest neighbor interactions and the neglect of overlap integrals, the electronic energies allowed for the 2D lattice are written as $e(k_a, k_b) = \alpha + 2\beta_a \cos(k_a a) + 2\beta_b \cos(k_b b)$, where α is the energy of the site orbital, and β_a and β_b are the nearest neighbor transfer integrals along the a and b directions, respectively. The wave vectors $k \equiv (k_a, k_b)$ can have any value within the first Brillouin zone defined by $-a^*/2 \leq k_a \leq a^*/2$ and $-b^*/2 \leq k_b \leq b^*/2$ (see Figure 1b where $\Gamma = (0, 0)$, $X = (a^*/2, 0)$ and $Y = (0, b^*/2)$, $a^* = 2\pi/a$ and $b^* = 2\pi/b$). For the rectangular 2D lattice, the directions of the reciprocal vectors a^* and b^* are the same as those of the repeat vectors a and b, respectively. The difference between two successive $e(k_a, k_b)$ values is very small so that the complete set of energies given by the previous equation is a continuous set of energy levels called a band.

In the context of one-electron band theory, where electron−electron repulsion is neglected so that each band level can be filled with two electrons, a metal is defined as a system that has at least one partially filled band. Thus, there is no energy gap between the highest occupied level (i.e., the Fermi level e_f) and the lowest unoccupied level. Suppose that the 2D lattice represents an ideal 1D system so that $\beta_a \neq 0$ and $\beta_b = 0$; that is, there is no intersite interaction along the b-direction, and so the 2D lattice is an assembly of noninteracting chains running along the a-direction. Then, the $e(k)$ versus k plot is dispersive along the chain direction (see $\Gamma \rightarrow X$) but dispersionless along the interchain direction (see $\Gamma \rightarrow Y$), as illustrated in Figure 1c. With one electron per site, the bottom half of the allowed energy levels are each doubly occupied to form

a metallic state (the dashed line in Figure 1c represents the Fermi level). For a 2D lattice with non-negligible intersite interactions along both *a* and *b* (i.e., β_a, $\beta_b \neq 0$), the band will be dispersive along both *a** and *b**.

For a partially filled band, some of the wave vectors of the Brillouin zone are associated with occupied energy levels and some with unoccupied energy levels. The boundary surface separating the occupied wave vectors from unoccupied wave vectors is called the Fermi surface (of course, in a 2D representation one should talk about a Fermi line). The Fermi surface associated with the half-filled band of Figure 1c is shown in Figure 1d. It consists of two parallel lines perpendicular to the chain direction. Carriers of metals are those electrons at the Fermi level. When a certain wave vector direction does not cross the Fermi surface (e.g., $\Gamma \rightarrow Y$ in Figure 1d) there are no electrons at the Fermi level having momentum along that direction so that the system is not metallic along that direction (i.e., the *b*-direction in real space). The Fermi surface of Figure 1d does not contain closed loops and hence corresponds to a 1D metal along the *a*-direction. Depending on the relative values of the transfer integrals and thus, the dispersion of the bands along different directions, there are different types of Fermi surfaces. For instance, the Fermi surface can contain closed loops (see Figure 1e) and then, the system is a 2D metal. The Fermi surface of Figure 1f represents an intermediate situation, that is, it is an open Fermi surface but with warped lines. It corresponds to a pseudo-1D metal along the *a*-direction; that is, a system with somewhat coupled chains along the *a* direction.

In addition to the dimensionality of metallic properties, Fermi surfaces are also important in explaining the electronic instabilities of systems with partially filled bands.[10] When a piece of a Fermi surface can be translated by a vector *q* and superimposed on another piece of the Fermi surface, the Fermi surface is said to be nested by the vector *q*. An example of a perfectly nested Fermi surface is that of Figure 1d. Metals with nested Fermi surfaces are susceptible to a modulation with wave vector *q* of their charge or spin density, which destroys the nested portions of the Fermi surface. Thus, if the nesting is complete, after the appearance of the modulation, the entire Fermi surface has been destroyed. The system exhibits a metal-to-insulator transition. If the nesting is only partial, part of the Fermi surface will remain after the appearance of the modulation and the transition will be of the metal-to-metal type. Metal-to-insulator transitions associated with such charge-density or spin-density waves (CDW or SDW) are frequently observed at low temperature in 1D or pseudo-1D metals.

Finally, it must be recalled that our discussion has been limited to the case where a delocalized description of the electrons is valid. This is the case when the bandwidth (*W*) is large compared with the on-site repulsion (*U*). When $U > W$, the electrons prefer to be localized on lattice sites.[12] In that case, the conductivity is activated because electron hopping from one site to the other leads to a situation in which two electrons reside on a single site, thereby causing on-site repulsion. Thus, if the dispersion of the band in Figure 1c is small compared with the on-site repulsion, the system will prefer to have one electron localized in each site of the lattice and it will be a semiconductor. In some low-dimensional metals, the bandwidth and on-site repulsion are comparable so that there can be a competition between the delocalized (i.e., metallic) and localized (i.e., semiconducting) electronic states. In that case, at a certain temperature, the metallic system can undergo a metal-to-semiconductor transition that is different in nature from those discussed before. Disorder, throughout the random potential it introduces, is another important factor favoring localized states in low-dimensional metals and more specially in molecular conductors.

Structural versus Electronic Dimensionality in Transition Metal Oxides and Bronzes with Partially Filled t_{2g}-Bands

Low-dimensional transition metal oxides and bronzes with partially filled t_{2g}-bands have been the subject of many studies during the past decade.[9d,9e,10,13−17] Some of these systems have been known for quite a long time, but their low-dimensional behavior had not been explored. In particular, molybdenum oxides and bronzes have atracted the interest of the solid-state community because of the physical properties they exhibit associated with their electronic instabilities. The blue bronzes $A_{0.3}MoO_3$ (A = K, Rb, Tl), the purple bronzes $A_{0.9}Mo_6O_{17}$ (A = Li, Na) and AMo_6O_{17} (A = K, Tl), as well as the Magnéli phases Mo_4O_{11}, Mo_8O_{23}, and Mo_9O_{26} have been carefully studied.[9d,9e,10,13,14] More recently, the large family of monophosphate tungsten bronzes has also received a lot of attention.[15−20] From the structural viewpoint, all these systems are 2D or 3-dimensional (3D) materials, but several of them behave as if they were 1D or pseudo-1D in terms of their physical behavior.

Many of these solids contain transition metal−oxygen layers made up of edge- and corner-sharing MO_6 octahedra and have large and complex unit cells. Here we will consider several of these materials with transition metal atoms with low average d electron count (i.e., d^1 or smaller). For the systems with several nonequivalent transition metal atoms in the unit cell, only a certain number of transition metal atoms can have d electrons and thus become responsible for their metallic properties. Thus, to understand the low-dimensional properties of these systems we must be able to identify, on the basis of the crystal structure, what transition metal atoms possess the d electrons. In some cases, just on the basis of such approach, the fact that the solid can exhibit a physical behavior suggestive of a dimensionality that is lower than expected on the basis of the crystal structure, can be understood.[10] However, this is only a first step in trying to understand the properties of these solids. To clarify the origin of their electronic instabilities, we must also be able to qualitatively build the band structure and thus, the Fermi surface, on the basis of the structural information.[10] In the following discussion we present several examples illustrative of such approach.

Let us start considering the simple MO_4 layer (see Figure 2a) that can be formed from MO_6 octahedra by sharing the four equatorial oxygen atoms (O_{eq}). The t_{2g}-block band structure of this layer can be understood in an extremely simple way. The d-block band levels of a crystal structure obtained by sharing octahedral corners are raised in energy when the orbitals of the bridging oxygen atoms are allowed by symmetry to mix with the metal d orbitals. Thus, all that should be done to evaluate the dispersion of the bands is just count how many oxygen p orbital contributions can be found in the crystal orbitals for different points of the Brillouin zone. With the system of axes shown in Figure 2a, the t_{2g}-orbitals are xy, xz, and yz. The crystal orbitals for the xy orbital at Γ, X, and M are shown in structures **1a**−**c**, where dots indicate the absence of oxygen p orbitals.

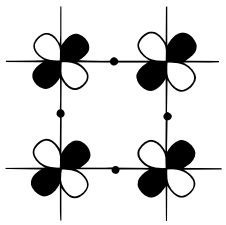

1a

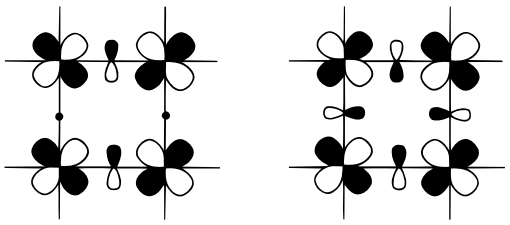

1b 1c

Those for the xz and yz orbitals are shown in **2a**−**c** and **3a**−**c**, respectively.

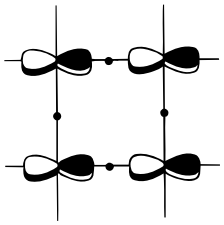

2a

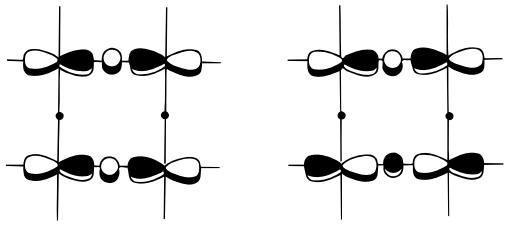

2b 2c

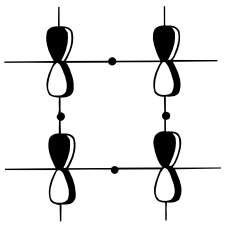

3a

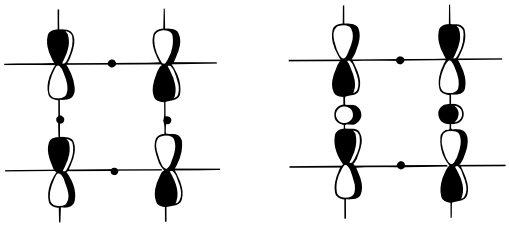

3b 3c

The qualitative band diagram can only be obtained if the oxygen contributions from the axial oxygen atoms (O_{ax}, see Figure 2a) are also taken into account. For simplicity, these axial contributions are not shown in **1**−**3**. However, it is obvious that there are two axial contributions per metal atom in **2a**−**c** and **3a**−**c** but none in **1a**−**c**. The total number of oxygen antibonding contributions per unit cell to the xy, xz, and yz crystal orbitals are summarized in Table 1, where Y/N and y/n indicate the presence/absence of such contributions in the bridging and axial oxygen positions, respectively. As shown elsewhere,[10] the energy destabilization of an oxygen p contribution in the bridging (Y) and axial (y) positions are related through the relationship $Y \approx 4y$. Thus, a qualitative band structure for the MO_4 single octahedral layer can be obtained (**4**) by counting the total number of oxygen contributions and using that relation.[21,22]

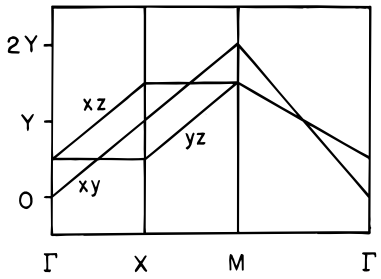

4

Several important conclusions can be drawn from **4** if we keep in mind that because of the low d electron count we are mainly interested in the bottom portion of the t_{2g}-block bands. First, we note that the lowest energy crystal orbital states occur around the special point Γ, and that these states are located in the xy band. Second, the electronic energy band derived from this orbital has significant dispersion in both directions of the layer. Third, the xz band is dispersive only along Γ−X (i.e., along the *a**-direction). Fourth, the yz band is dispersive only along Γ−Y (i.e., the *b**-direction). In conclusion, the t_{2g}-block band structure of the MoO_4 layer is the superposition of a 2D band and two 1D bands along the *a*- and *b*-directions. The lowest lying

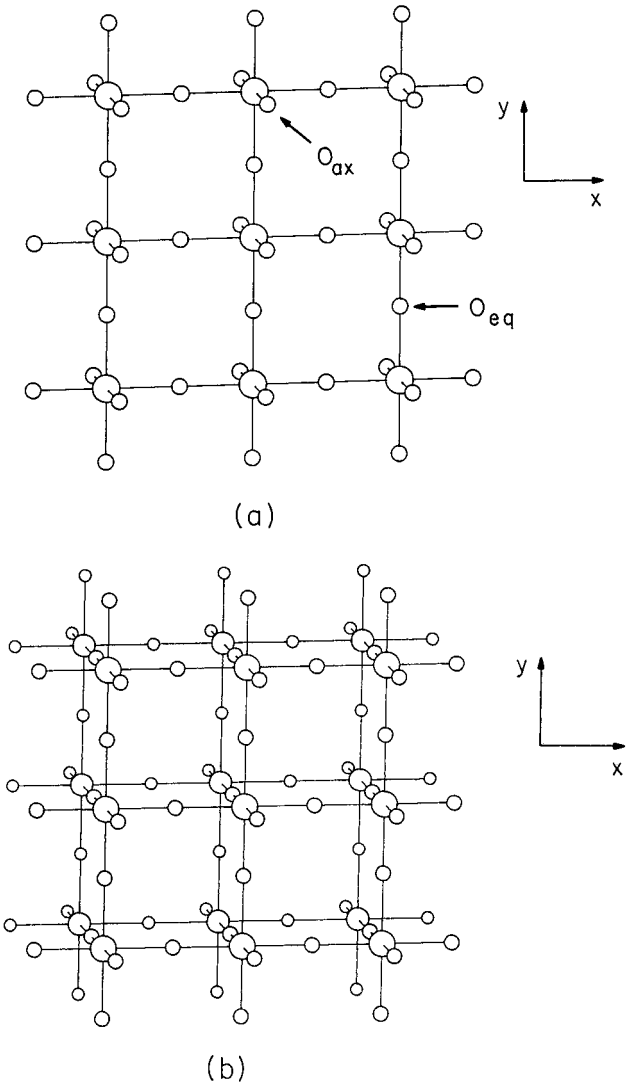

Figure 2. (a) MO_4 layer generated by equatorial oxygen sharing of MO_6 octahedra. (b) M_2O_7 double layer generated from the MO_4 layers by axial oxygen sharing.

Table 1. Antibonding Contributions per Unit Cell of the Oxygen p Orbitals in the t_{2g}-Block Bands of the MO_4 Octahedral Lattice of Figure 2a

band	crystal orbital	wave vector point	bridging contributions	axial contributions
xy	**1a**	Γ	NN	nn
	1b	X	YN	nn
	1c	M	YY	nn
xz	**2a**	Γ	NN	yy
	2b	X	YN	yy
	2c	M	YN	yy
yz	**3a**	Γ	NN	yy
	3b	X	NN	yy
	3c	M	NY	yy

levels of the t_{2g}-block band are those of the 2D band. These results can, however, be affected by the nature of any octahedral distortion and the possible layer condensations leading to more complex lattices.

Let us first consider the case of the M_2O_7 double octahedral layers present in the structure of $Sr_3V_2O_7$.[23] The M_2O_7 double layers can be formed from two MO_4 layers by sharing their axial oxygen atoms (see Figure 2b). The octahedra in the Sr_2O_7 double layers are quite regular. For instance, the nonbridging M−O_{ax} bond length is only 0.048 Å shorter than the average M−O bond distance. Thus, the band structure of the Sr_2O_7 double layer can be constructed just by considering the effect of the layer condensation on the qualitative results of **4**. This is in fact quite simple. The orbitals of each M−O_{ax}−M linkage leading to the six t_{2g}-block bands are shown in **5a**−**b**, **6a**−**b**, and **7a**−**b** (for simplicity, the contributions of the nonbridging O_{ax} orbitals are not shown in **5**−**7**).

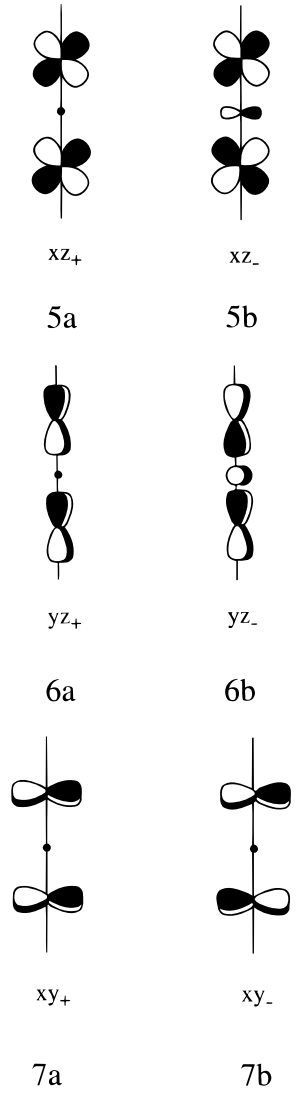

The xy_+ (**7a**) and xy_- (**7b**) combinations are practically degenerate because the bridging p orbitals of the O_{ax} atom cannot interact with the xy orbitals due to the δ symmetry along the M−O_{ax}−M axis. The number of oxygen p orbital contributions per unit cell of the double octahedral layer to the xy_+ and xy_- bands are thus identical and just twice those of the single octahedral layer. The xz_+ (**5a**) and yz_+ (**6a**) combinations are lower than the xz_- (**5b**) and yz_- (**6b**) because they do not have p orbital contributions at the bridging axial position. The number of oxygen p orbital contributions per unit cell of the double octahedral layer to the xz_+ and yz_+ bands are twice those of the single octahedral layer minus two axial contributions ($2y = Y/2$). Those of the xz_- and yz_- bands are the same as those of the xz_+ and yz_+ bands plus one bridging contribution (Y) coming from the M−O_{ax}−M position. Thus, the qualitative

band structure for the double octahedral layer can be easily constructed and is shown in **8**.

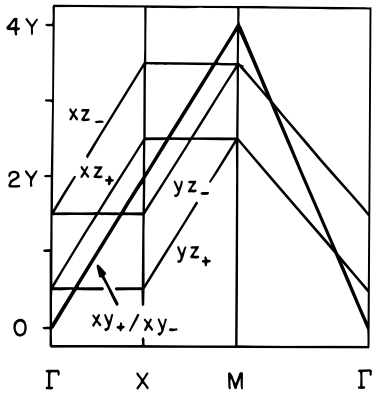

8

With the oxidation states O^{2-} and Sr^{2+}, the vanadium atoms in the V_2O_7 layers of $Sr_3V_2O_7$ have a d^1 electron count. Thus, we are only interested in the lowest part of the t_{2g}-block band structure that occurs around the Γ point. As clearly shown by the qualitative construction, the only difference between the band structures of the single and double layers around Γ is that there are two 2D bands in the case of the double layer instead of just one for the single layer. Thus, the four main conclusions of the study of the single layer are still applicable here. The calculated results using the actual structure of the Sr_2O_7 double layers in $Sr_3V_2O_7$ are shown in Figure 3a.[21,24] The agreement with the qualitative model is almost perfect. Because there are two electrons to fill the bands of Figure 3a and the bottom of the 1D bands are very near the bottom of the 2D bands, it is most likely that the Fermi level will cross both types of bands. Thus it is predicted that the Fermi surface of this system will contain two closed 2D portions and two sets of parallel lines (1D portions) perpendicular to the *a*- and *b*-directions, respectively. The calculated Fermi surface[21,24] is shown in Figure 3b and is in complete agreement with the previous analysis. Thus, the Fermi surface of the double octahedral layers in $Sr_3V_2O_7$ contains both 2D and 1D contributions and this result can be understood on a purely qualitative basis.

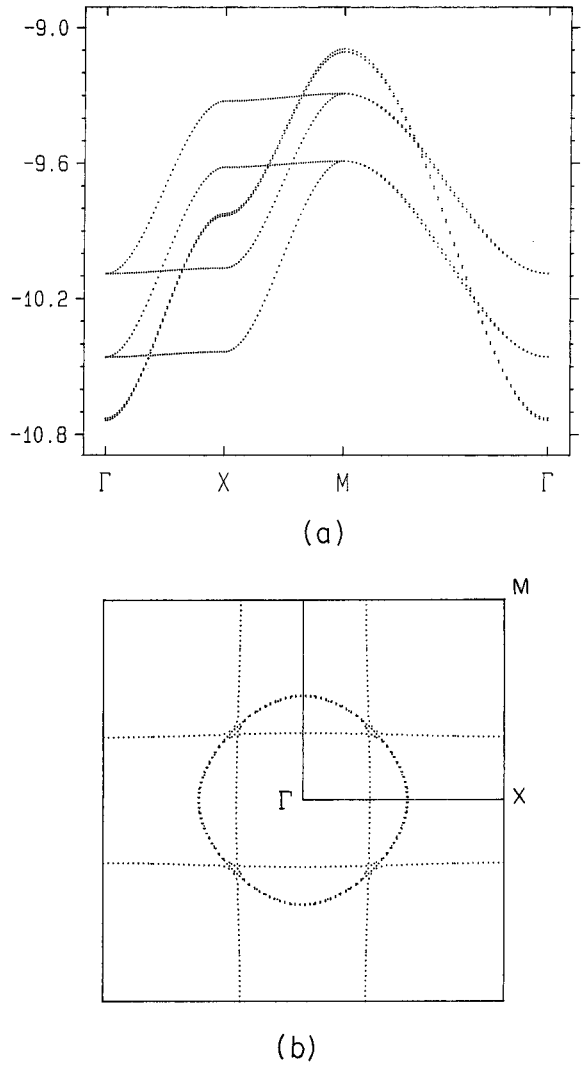

Figure 3. The (a) t_{2g}-block band structure and (b) Fermi surfaces calculated for the V_2O_7 double octahedral slabs of $Sr_3V_2O_7$. Γ, X, and M refer to the wave vectors (0, 0), (*a**/2, 0), and (*a**/2, *a**/2), respectively, where *a* is the repeat vector of the square lattice.

To progress we must now slightly digress and consider the effect on the t_{2g}-orbitals of the octahedral distortions more frequently encountered in these materials. The t_{2g} levels of a regular MoO_6 octahedron have antibonding combinations between the Mo d orbitals and the O p orbitals. Hence, a shortening of an Mo−O bond length raises the energy of any t_{2g}-orbital if it has an antibonding combination between the Mo and O orbitals along the shortened Mo−O bond. Consequently, a distortion where one Mo−O bond is shortened leaves one t_{2g} level (i.e., that which is in a plane perpendicular to the shortened Mo−O bond) and raises the energy of the remaining two levels (see **9**).

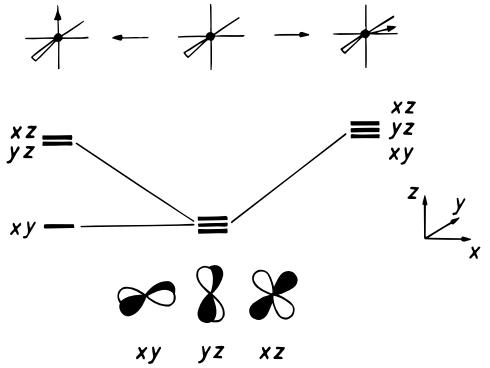

9

By contrast, all three t_{2g} levels are raised by a distortion in which two or more Mo−O bonds are shortened. Thus, inspection of the nature and extent of the octahedral distortions allows the prediction of which octahedra of a given oxide lattice would have d electrons and what kinds of occupied (or partially occupied) t_{2g}-block bands the oxide is likely to have.[10]

A different type of double octahedral layer can be constructed when every octahedra of one MO_4 layer shares two edges with the octahedra of the other layer (see Figure 4a). For instance, these MO_3 double layers are found in $H_{0.33}MoO_3$.[25] It is of interest to briefly consider this system because it exhibits a metal-to-insulator transition at 380 K, associated with the appearance of a $3a \times 6c$ superlattice, which has been proposed to originate from an electronic instability.[25]

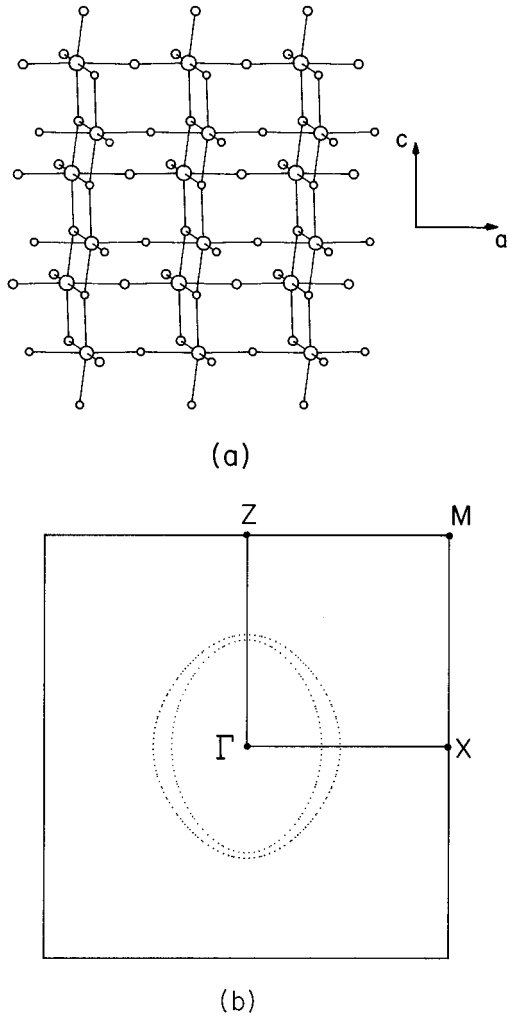

Figure 4. The (a) MoO_3 double octahedral layers in $H_{0.33}MoO_3$ and (b) Fermi surface calculated for $H_{0.33}MoO_3$ before the appearance of the $3a \times 6c$ superstructure. Γ, X, Z, and M refer to the wave vectors (0, 0), ($a^*/2$, 0), (0, $c^*/2$), and ($a^*/2$, $c^*/2$), respectively.

The octahedra in $H_{0.33}MoO_3$ are strongly distorted. There is a strong bond alternation in the direction perpendicular to the layer. Thus, the Mo−O bond length associated with the non-shared O atom is very short (1.69 Å) compared with that of the shared O atom (2.33 Å). Thus, only the t_{2g}-orbital that is δ with respect to the bond length alternation (i.e., the in plane t_{2g}-orbital) will remain low in energy.

Now, to qualitatively build the band structure of the MoO_3 double layers[22] in $H_{0.33}MoO_3$ we must separately consider the effect of the octahedral distortion and the layer condensation. Because of the octahedral distortion, the 1D bands (see **4**) of the single octahedral layer will be strongly raised in energy and the 2D band will be left at the bottom of the band structure. The in-plane t_{2g}-orbital is δ with respect to the Mo−O direction perpendicular to the layers, so the 2D band of every single layer remains unaffected by the condensation. The situation could be different for the two out-of-plane t_{2g}-orbitals. Because two of their lobes point toward Mo atoms of the other layer along the *c*-direction (see Figure 4a), it could be thought that they could lead to Mo−Mo bonding and antibonding interlayer combinations. If the energy stabilization afforded by the Mo−Mo bonding interactions were strong enough to compensate for the destabilization afforded by the octahedral distortion, one of the four 1D bands of the double layer could be in the same energy range as the two 2D bands. However, inspection of the inner structure of the double layer shows that this is not possible for two reasons. First, because of the bond length alternation, the Mo−Mo distance is quite long. Second, the Mo atoms move a little bit out of the plane of the equatorial oxygen atoms toward the non-shared oxygen atom. This movement leads to a rehybridization as shown in **10**, which further reduces the Mo−Mo already weak interaction.

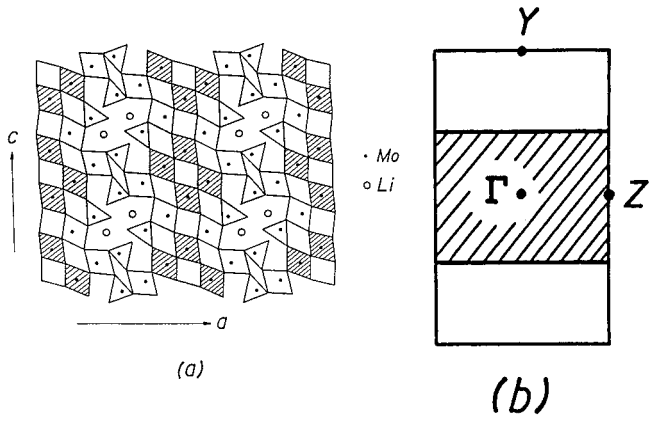

Figure 5. (a) Schematic drawing of the crystal structure of $Li_{0.9}Mo_6O_{17}$, where each triangle or tetragon with an Mo atom represents an MoO_4 tetrahedron or MoO_6 octahedron, respectively. (b) Calculated Fermi surface for $Li_{0.9}Mo_6O_{17}$. Γ, Y, and Z refer to the wave vectors (0, 0), ($b^*/2$, 0), and (0, $c^*/2$), respectively.

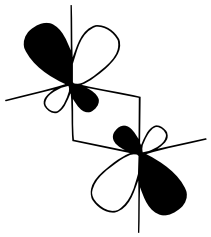

10

This analysis leads to the prediction that the two practically independent 2D bands will be at the bottom part of the t_{2g}-block band structure and thus will be partially filled with 0.66 electrons. Thus, the Fermi surface is predicted to be made of two practically identical closed loops around the Γ point. This prediction is in excellent agreement with the calculated Fermi surface shown in Figure 4b.[22] Because this Fermi surface does not exhibit nesting vectors, the metal-to-insulator transition of $H_{0.33}MoO_3$ cannot be due to a Fermi surface-driven instability. Most likely it is due to an order−disorder phenomena of the protons.

The type of analysis developed here has wide applicability in the study of low-dimensional transition metal oxides and bronzes with partially filled t_{2g}-block bands.[10] As a final example, let us briefly consider the structurally more complex case of the lithium purple bronze $Li_{0.9}Mo_6O_{17}$.[26] This bronze has a 3D crystal structure but exhibits pseudo-1D type conductivity and eventually becomes superconducting at 2 K.[26,27] $Li_{0.9}Mo_6O_{17}$ has 2.9 electrons per six molybdenum atoms and consequently, only the bottom portion of the t_{2g}-block bands can be filled. As shown in Figure 5a, $Li_{0.9}Mo_6O_{17}$

contains a 3D network of Mo−O bonds made of octahedral layers connected through MoO_4 tetrahedra. The Li atoms reside in the open channels left free between the layers.[26]

The octahedral layers of $Li_{0.9}Mo_6O_{17}$ have four different types of molybdenum atoms: Mo^{I}, Mo^{II}, Mo^{III}, and Mo^{IV}. The different MoO_6 octahedra in these layers share six to three of their oxygen atoms with MoO_6 octahedra and the remaining ones with MoO_4 tetrahedra. Consequently, each MoO_6 octahedron can be classified as an (m + n) octahedron, where m and n are the number of oxygen atoms shared with MoO_6 octahedra and MoO_4 tetrahedra, respectively. Then, the four different molybdenum atoms Mo^{I} to Mo^{IV} are associated with octahedra of types (5 + 1), (6 + 0), (4 + 2) and (3 + 3), respectively (see Figure 5a). The MoO_4 tetrahedra have in average much shorter Mo−O bonds than do the MoO_6 octahedra. All octahedra of the structure have three short and three long Mo−O distances. However, the short Mo−O bonds of the (3 + 3) and (4 + 2) octahedra are shorter than those of the (5 + 1) and (6 + 0) octahedra. Therefore, the lowest lying d-block bands of $Li_{0.9}Mo_6O_{17}$ are expected to be largely represented by the t_{2g}-levels of the (5 + 1) and (6 + 0) octahedra (i.e., the t_{2g}-levels of Mo^{I} and Mo^{II}). These two types of octahedra are hatched in Figure 5a. Therefore, according to the crystal structure analysis, the lowest lying d-block bands of $Li_{0.9}Mo_6O_{17}$ would be given by the t_{2g}-block bands of the isolated Mo_4O_{18} chains singled out in Figure 5a. Hence, $Li_{0.9}Mo_6O_{17}$ is expected to exhibit pseudo-1D electrical properties. Thus, just on the basis of an analysis of the crystal structure, the pseudo-1D electrical behavior of $Li_{0.9}Mo_6O_{17}$ can be easily understood. The calculated Fermi surface, reported in Figure 5b, consists of two superposed pairs of parallel lines perpendicular to the *b**-direction, which is in agreement with the fact that the Mo_4O_{18} chains run along the *b*-direction (see Figure 5a). The Fermi surface of Figure 5b is in excellent agreement with the results of angle-resolved photoemision experiments.[28] An orbital interaction analysis similar to that presented for the double octahedral lattices can be easily carried out and leads to a qualitative band structure and Fermi surface, which again are in excellent agreement with the calculated results. This analysis has been reported in detail elsewhere.[10,29]

Many examples of the application of this type of analysis to low-dimensional metals with partially filled t_{2g}-block bands have been reported in the literature and have provided quite a good understanding of otherwise puzzling observations.[10] It is clear that very simple ideas based on overlap, symmetry, and chemical bonding arguments can lead to very good qualitative band structures and Fermi surfaces for this class of materials and thus provide a simple yet very powerful tool to understand their electronic structures and the origin of their interesting behavior.

Hydrogen Bonding and Transport Properties of Molecular Conductors: The Story of the (BEDT-TTF)$_4$Re$_6$Se$_5$Cl$_9$·[Guest] [Guest = Dimethylformamide (DMF), Tetrahydrofuran (THF), Dioxane] and Related Salts

The exploration of the lattice architectures that can be obtained when organic radical cations are associated with large all-inorganic anions pioneered by Batail and his group[30] has opened a fruitful new direction in the search for low-dimensional molecular solids.[31] Here we would like to discuss the (BEDT-TTF)$_4$Re$_6$Se$_5$Cl$_9$·[guest] (BEDT-TTF = (bis(ethylenedithio (tetrathiafulvalene),

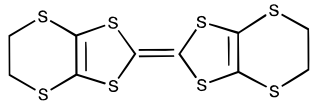

11

BEDT-TTF

11, guest = DMF, THF, dioxane) series of salts,[32] to explore some of the strategies that can be used when trying to tune the transport properties of low-dimensional molecular conductors.

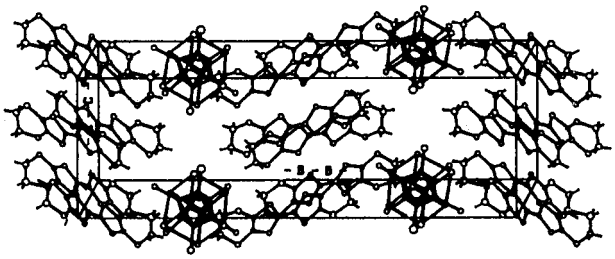

Figure 6. Crystal structure of *m*-(BEDT-TTF)$_4$Re$_6$Se$_5$Cl$_9$·[DMF]. The DMF guest molecules are not shown.[32]

The simplest strategy consists of changing some of the transfer integrals of the lattice. The crystal structure of *m*-(BEDT-TTF)$_4$Re$_6$Se$_5$Cl$_9$·[DMF] is shown in Figure 6. It consists of layers of BEDT-TTF donors alternating with layers of the $Re_6Se_5Cl_9^-$ cluster. As shown in Figure 6, between the cluster anions remains some empty space. Solvent molecules (not shown in Figure 6 for clarity) occupy these holes and give cohesion to the structure. It is important to realize that several of the hydrogen atoms of the BEDT-TTF donor point toward the solvent position and thus the donor layer and the solvent molecules are related through hydrogen bonds. Thus, the possibility of changing the internal structure of the donor layers (and thus, some of the transfer integrals) by appropriately replacing the solvent molecules immediately comes to mind.

The calculated band structure near the Fermi level for the donor layers of *m*-(BEDT-TTF)$_4$Re$_6$Se$_5$Cl$_9$·[DMF] is shown in Figure 7a. The unit cell of the donor layer contains four molecules, so there are four bands mainly derived from the BEDT-TTF highest occupied molecular orbital (HOMO). With the average charge required by the stoichiometric formula [i.e., $(BEDT\text{-}TTF)^{+1/4}$], there are seven electrons to fill these bands. As shown in Figure 7a, the Fermi level associated with this filling cuts only the highest of the four bands which, consequently, is half filled. The partially filled band is dispersive along both the *a**-(i.e., Γ → X) and *c**-(i.e., Γ → Z) directions. However the dispersion along *a** is smaller so that the Fermi level does not cut the band along this direction, leading to the open Fermi surface shown in Figure 7b. According to this result, *m*-(BEDT-TTF)$_4$Re$_6$Se$_5$Cl$_9$·[DMF] is a pseudo-1D metal.

Interestingly, at the X point, the dispersion curve shows a minimum that lies very near to the Fermi level (∼ 0.03 eV). A slight perturbation of the lattice affecting

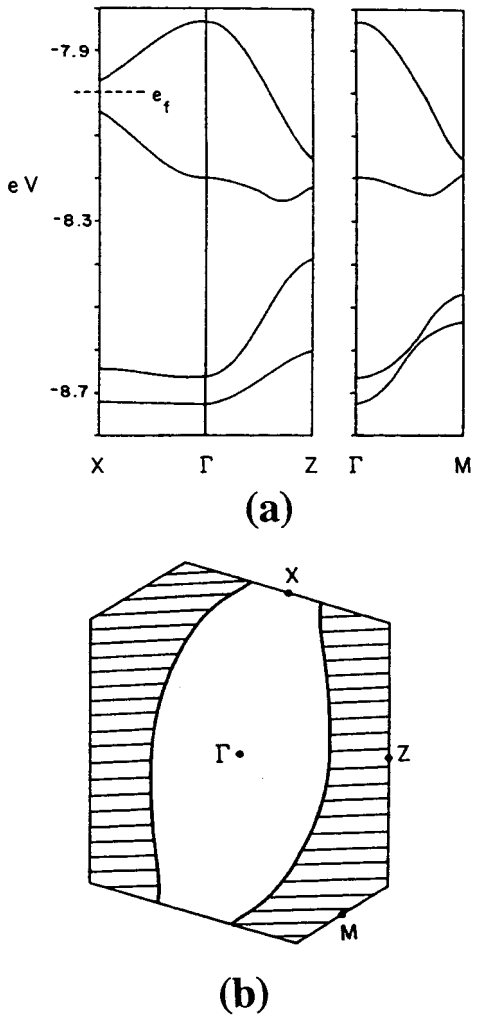

Figure 7. (a) Calculated band structure and (b) Fermi surface for *m*-(BEDT-TTF)$_4$Re$_6$Se$_5$Cl$_9$·[DMF]. The dashed line in (a) indicates the Fermi level. Γ, X, Z, and M refer to the wave vectors (0, 0), (*a**/2, 0), (0, *c**/2), and (-*a**/2, *c**/2), respectively. In b, the wave vectors of the shaded and unshaded regions refer to filled and unfilled band levels, respectively.

the transfer integrals could result with the Fermi level cutting the band also along the *a**-direction and thus leading to a closed 2D Fermi surface. In this process, the X point becomes the locus of a van Hove singularity in the density of states, so the physical properties of this type of materials should be very exciting to study. The question is: How to induce these perturbations? With the structural information in mind, it is clear that by changing the nature of the guest molecules filling the cavities between the clusters, slight displacements of the BEDT-TTF molecules will be induced through hydrogen bonding. Thus, for this particular lattice, there is the possibility of changing the electronic structure (and thus the transport properties) by using different types of solvent molecules.

Following this reasoning, four different salts of this type could be prepared: *m*-(BEDT-TTF)$_4$Re$_6$Se$_5$Cl$_9$·[DMF], *t*-(BEDT-TTF)$_4$Re$_6$Se$_5$Cl$_9$·[DMF], (BEDT-TTF)$_4$Re$_6$Se$_5$Cl$_9$·[THF], and (BEDT-TTF)$_4$Re$_6$Se$_5$Cl$_9$·[dioxane].[32] Indeed, the internal structure of the donor slabs of these salts shows noticeable differences although the main architecture is kept. The calculated Fermi surfaces for *t*-(BEDT-TTF)$_4$Re$_6$Se$_5$Cl$_9$·[DMF] and (BEDT-TTF)$_4$Re$_6$Se$_5$Cl$_9$·[dioxane] are shown in Figures 8a and 8b, respectively. Although the Fermi surfaces of *m*-(BEDT-TTF)$_4$Re$_6$Se$_5$Cl$_9$·[DMF] (Figure 7b) and (BEDT-TTF)$_4$Re$_6$Se$_5$Cl$_9$·[dioxane] (Figure 8b) are open, that of *t*-(BEDT-TTF)$_4$Re$_6$Se$_5$Cl$_9$·[DMF] (Figure 8a) is closed. Thus, it is clear that without disturbing the main architecture of the lattice, just by appropriately changing the nature of the guest molecules, we can change the topology of the Fermi surface and thus modify the transport properties of the system. Hydrogen bonding plays a fundamental role in this process.

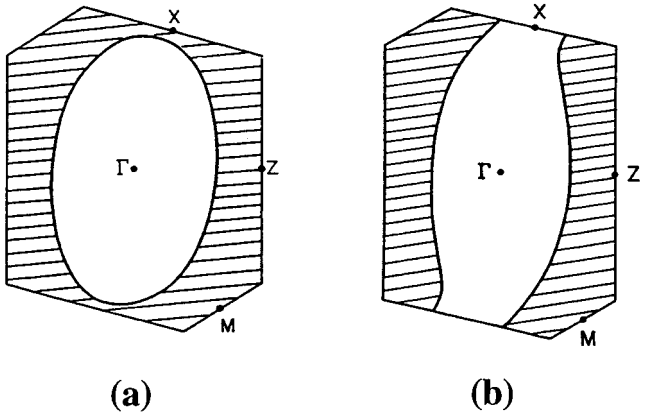

Figure 8. Fermi surface calculated for (a) *t*-(BEDT-TTF)$_4$Re$_6$Se$_5$Cl$_9$·[DMF] and (b) (BEDT-TTF)$_4$ Re$_6$Se$_5$Cl$_9$·[dioxane]. The wave vectors of the shaded and unshaded regions refer to filled and unfilled band levels, respectively.

There is another aspect of the strategy just outlined that deserves comment. Depending on the nature and shape of the guest molecule, the size and hydrogen bonding requirements of the cavity can be fulfilled to a different extent. Thus, the guest molecule will have some freedom degree within the cavity and this can lead to some disorder. For instance, it was the recognition of inversion disorder of the solvent molecule that prompted the choice of dioxane as a possible guest molecule to reduce such disorder. Indeed, (BEDT-TTF)$_4$Re$_6$Se$_5$Cl$_9$·[dioxane] has a highly ordered structure. Because it is well known that disorder can have a strong influence on the conductivity of molecular metals, this affords another strategy to slightly change the transport properties of this lattice. It is expected that when the degree of disorder decreases, the probability to have electron localization, and thus activated conductivity, will also decrease.

The degree of disorder decreases from m-(BEDT-TTF)$_4$Re$_6$Se$_5$Cl$_9$·[DMF], to (BEDT-TTF)$_4$Re$_6$Se$_5$Cl$_9$·[THF] and to (BEDT-TTF)$_4$Re$_6$Se$_5$Cl$_9$·[dioxane], something that is easily understandable in terms of the nature and shape of the different guest molecules. This is nicely reflected in the conductivity of these salts. All of them exhibit high room-temperature conductivity and metallic behavior. When the temperature is decreased, an activated behavior appears in a temperature range that decreases with the amount of disorder in the structure. A broad minimum in the resistivity curve is observed at ~90 K for *m*-(BEDT-TTF)$_4$Re$_6$Se$_5$Cl$_9$·[DMF], the most severely disordered material. It is shifted down to 50 K for (BEDT-TTF)$_4$Re$_6$Se$_5$Cl$_9$·[THF] and has essentially vanished in (BEDT-TTF)$_4$Re$_6$Se$_5$Cl$_9$·[dioxane].[32] Es-

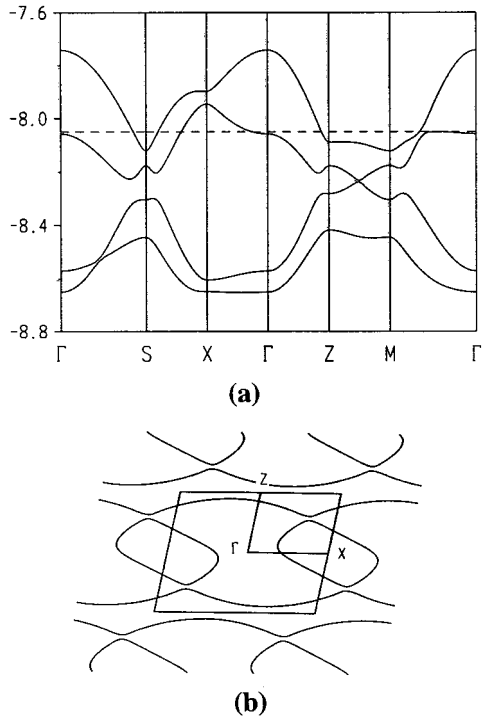

Figure 9. (a) Band structure and (b) Fermi surface for the donor layers of (BEDT-TTF)$_4$Re$_6$S$_6$Cl$_8$·[dioxane]. The dashed line in a indicates the Fermi level. Γ, X, Z, M, and S refer to the wave vectors (0, 0), (*a**/2, 0), (0, *c**/2), (*a**/2/, *c**/2), and (-*a**/2, *c**/2), respectively.

sentially, changing the nature of the guest molecule allowed the suppression of the metal-to-insulator transition.

There is still another possibility to modify the transport properties of this type of lattice. As shown by Batail and co-workers,[33] anions with practically the same shape but different charge can be prepared by changing the number of chalcogen and halogen atoms of the cluster. This result immediately suggests the possibility of changing the number of the electrons filling the HOMO bands of the donor lattice. This possibility has actually been realized and several salts with dianions, such as $Re_6S_6Cl_8^{2-}$ or $Re_6Se_6Cl_8^{2-}$, have been prepared.[34] The donor lattices of these salts are very similar to those of the monoanions. Consequently, it is expected that the band structures will also be very similar and that the change in the transport properties will be just due to the different filling of the bands.

The calculated band structure and Fermi surface of the (BEDT-TTF)$_4$Re$_6$S$_6$Cl$_8$·[dioxane] salt are shown in Figure 9.[34] The band structures of Figures 9a and 7a are indeed very similar (the band structure of the (BEDT-TTF)$_4$Re$_6$Se$_5$Cl$_9$·[dioxane] salt, although of course not identical, is in fact quite similar to that of Figure 7a and thus is not shown). Compare for instance lines Γ → X and Γ → Z in the two figures (note also that Γ → M in Figure 7a corresponds to Γ → S in Figure 9a). However, because of the smaller number of electrons filling these bands, the Fermi level cuts now two bands instead of just one, which leads to a Fermi surface for (BEDT-TTF)$_4$Re$_6$S$_6$Cl$_8$·[dioxane] (Figure 9b) that is very different in shape from that of (BEDT-TTF)$_4$Re$_6$Se$_5$Cl$_9$·[dioxane] (Figure 8b).

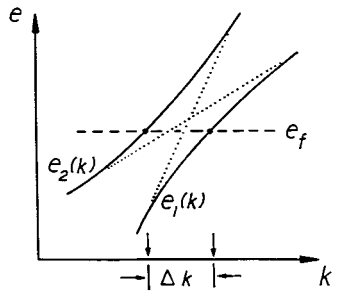

Figure 10. Schematic drawing of two band dispersion curves with an avoided crossing near the Fermi level.

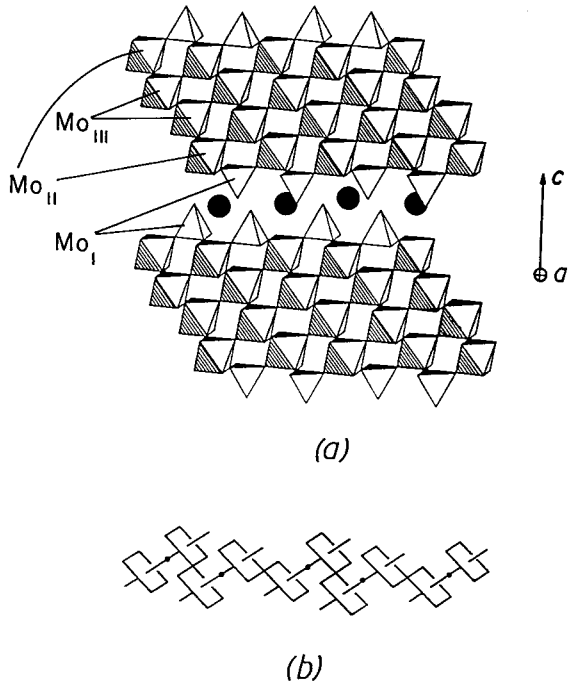

Figure 11. (a) Perspective view of two adjacent Mo_6O_{17} layers of KMo_6O_{17}. The *c*-axis is perpendicular to the layer and the *a*-axis is perpendicular to the plane of the drawing. (b) Schematic view of the inner Mo_2O_9 layer in KMo_6O_{17}.

The physical behavior of the two salts, (BEDT-TTF)$_4$Re$_6$S$_6$Cl$_8$·[dioxane] and (BEDT-TTF)$_4$Re$_6$Se$_5$Cl$_9$·[dioxane], is very different. Both salts are room-temperature metals but, whereas the latter keeps its metallic character down to very low temperatures, the former undergoes an abrupt metal-to-insulator transition at ~100 K, probably associated with some structural change. This transition can be suppressed under pressure.[34] Again, the physical properties and Fermi surfaces of the dianion salt, can be modified by changing the nature of the guest molecule. For instance, both (BEDT-TTF)$_4$Re$_6$Se$_6$Cl$_8$·[H$_2$O]$_2$ and (BEDT-TTF)$_4$Re$_6$S$_6$Cl$_8$·[H$_2$O]$_2$ are also room-temperature metals and have donor lattices very similar to that of (BEDT-TTF)$_4$Re$_6$S$_6$Cl$_8$·[dioxane], but none of them exhibits a metal-to-insulator transition like that of (BEDT-TTF)$_4$Re$_6$S$_6$Cl$_8$·[dioxane].

It is clear that this type of salts offer fascinating possibilities to finely modulate their transport properties. Carefully planned chemical changes can lead to modifications in (a) the strength of some transfer integrals of the lattice, (b) the electron filling of the bands, and (c) the degree of disorder. All of these changes have an important role in controlling the transport properties of the lattice.

Finding 1D Systems Where There Seem Not To Be: The Concept of Hidden Nesting

Analysis of the Fermi surface nesting requires a special consideration for a low-dimensional metal with several partially filled bands.[35] Figure 10 illustrates two band dispersion curves with an avoided crossing in the vicinity of the Fermi level. With increasing the extent of band hybridization, the separation Δk between the Fermi vectors becomes larger. In general, such avoided crossings in band dispersion surfaces lead to avoided crossings in the corresponding Fermi surfaces. Therefore, a low-dimensional metal with several partially filled bands may give rise to apparently unnested Fermi surfaces, although their intended surfaces (that is, those expected in the absence of the avoided crossings) are all nested. In such a case, the nesting is hidden by the avoided crossings. Such hidden, nested Fermi surfaces, can lead to CDWs thereby destroying the nested portions of the combined Fermi surfaces. Thus, to understand the CDW phenomenon of a low-dimensional metal with several partially filled bands, it is essential to search for a nesting in the intended, hidden Fermi surfaces.

The potassium purple bronze KMo_6O_{17} has separated Mo−O layers of composition Mo_6O_{17}, which are made up of both MoO_6 octahedra and MoO_4 tetrahedra (Figure 11). The sodium and thallium purple bronzes are similar in structure to the potassium purple bronze. The potassium purple bronze is a 2D metal above 120 K, at which temperature it undergoes a CDW phase transition.[14,36−38] It remains 2D metallic after this phase transition. Diffuse X-ray scattering and electron diffraction studies show the occurrence of superlattice spots at $a^*/2$, $b^*/2$, and $(a^* - b^*)/2$ below 120 K.[38] According to the thermoelectric power measurements, the major carriers for electrical transport are electrons and holes above and below 120 K, respectively. Hall effect measurements show that both electrons and holes are present below 120 K. According to these observations, several partially filled d-block bands are present in KMo_6O_{17}. In electrical, CDW, and other physical properties, the sodium and thallium purple bronzes are similar to KMo_6O_{17}.[37]

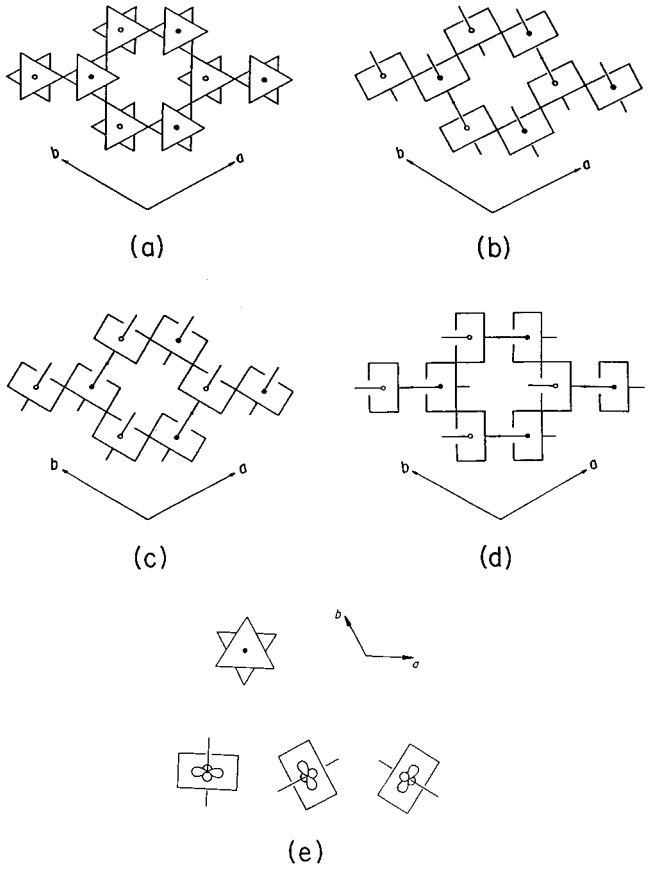

Figure 12. Schematic view of the Mo_2O_9 trigonal layer present in the purple bronze KMo_6O_{17}. The projection view perpendicular to the layer is shown in a. The Mo_2O_9 layer is constructed in terms of the Mo_2O_{10} zigzag chains running along the *a*-, *b*-, and $(a + b)$-directions in b, c, and d, respectively. Perspective views of the three t_{2g}-orbitals of an MoO_6 octahedron in the Mo_2O_9 layer are shown in e, where the d-orbital containing planes are aligned along the *a*-, *b*-, and $(a + b)$-directions of the Mo_2O_9 layer.

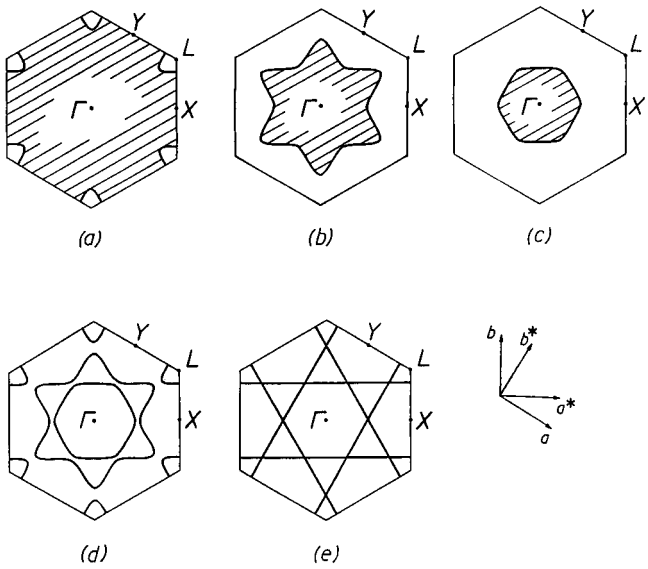

Figure 13. Hidden nesting in the purple bronze KMo_6O_{17}. The calculated Fermi surfaces for the three partially filled d-block bands are shown in a, b, and c, the combined Fermi surfaces are in d, and the hidden 1D Fermi surfaces are in e.

As shown in Figure 11a, there exist three different types of Mo atoms in AMo_6O_{17}.[39] According to both electronic band structure calculations[40] and a study of the bond-valence-sum analysis of the metal−oxygen bond lengths,[39] the d electrons of KMo_6O_{17} reside primarily in the MoO_6 octahedra of Mo_{III}. Consequently, the Mo_2O_9 layer formed by the inner two octahedral sublayers plays an important role in determining the electronic structure of KMo_6O_{17}. The Mo_2O_9 layer is schematically shown in Figure 11b. A projection view of the Mo_2O_9 layer along the *c*-axis is given in Figure 12a.

KMo_6O_{17} has three electrons per unit cell to fill its three lowest-lying d-block bands so that there are three partially filled d-block bands. The Fermi surfaces of the three bands are shown in Figures 13a, b, and c.[35] These surfaces are all 2D in nature, and their individual partial nesting does not explain the observed CDW vectors. The three surfaces are combined together in Figure 13d, which, upon neglecting the avoided crossings, can be decomposed into three sets of nested 1D surfaces, as illustrated in Figure 13e. The 1D Fermi

surfaces are perpendicular to the *a*-, *b*-, and (*a* + *b*)-directions of the trigonal lattice.

To a first approximation, therefore, the three partially filled bands of KMo_6O_{17} are derived from three 1D bands dispersive along the *a*-, *b*-, and (*a* + *b*)-directions. This conclusion is consistent with the structural and electronic properties of this bronze. As already mentioned, the conducting electrons are confined into the inner Mo_2O_9 layers (see Figures 11b and 12a). These layers can be constructed from Mo_2O_{10} zigzag chains, running along the *a*-, *b*-, or (*a* + *b*)-direction, by sharing their axial oxygen atoms, as shown in Figures 12b, c, and d. The partially filled bands of KMo_6O_{17} are made up of the t_{2g}-orbitals of MoO_6 octahedra. As illustrated in Figure 12e, the t_{2g}-orbitals are contained in the planes of the chains (that is, those defined by the equatorial oxygen atoms) running along the *a*-, *b*- and (*a* + *b*)-directions. Thus, the t_{2g}-orbitals are π-orbitals along the intrachain directions but δ-orbitals along the interchain directions. Consequently, the band associated with each of the t_{2g}-orbitals is dispersive along the associated intrachain direction but dispersionless along the associated interchain direction. In addition, due to the local orthogonality of the t_{2g}-orbitals, the three chain bands resulting from the t_{2g}-orbitals are practically independent of one another, to a first approximation.[10,35,40] Thus, for qualitative purposes, the bottom three d-block bands of KMo_6O_{17} can be approximated by the three independent 1D bands resulting from the t_{2g}-orbitals of each octahedra. It is these three "hidden 1D bands" that are responsible for the hidden nesting shown in Figure 13e.[35]

The electronic structure of KMo_6O_{17} is essentially represented by the three hidden 1D bands. Because there are three electrons to fill these bands, each band is half-filled. Consequently, the t_{2g}-block bands of KMo_6O_{17} can be viewed as a superposition of three almost independent half-filled 1D bands. It is this observation that led to the formulation of the concept of hidden nesting.[35]

As mentioned, a CDW formation introduces an additional periodicity of electron density distribution into the lattice, and hence gives rise to superlattice reflections in the X-ray or electron diffraction pattern below the CDW phase transition temperature T_p. At temperatures above T_p, a nested 1D Fermi surface leads to CDW fluctuations. The latter cause planar diffuse scattering and hence $2k_f$ diffuse lines between layers of main Bragg reflections in X-ray diffraction patterns.[38,41] Thus, like any 1D metallic system with CDW instability, KMo_6O_{17} was predicted[35] to show 1D CDW fluctuations above 120 K and hence diffuse lines in the X-ray patterns. As schematically shown in Figure 14, the diffuse lines resulting from the CDW fluctuations of the chains along the *a*-, *b*-, or (*a*+*b*)-direction should be perpendicular to the chain direction and are located at the midpoints between the rows of the main Bragg spots perpendicular to the chain direction. Thus, the three sets of the diffuse lines should form hexagons around each main Bragg reflection spot (Figure 14).

The pattern of the diffuse lines predicted by Figure 14 was observed by diffuse X-ray scattering experiments on AMo_6O_{17} (A = K, Na) at room temperature.[35] As the temperature is lowered below 120 K, the diffuse lines

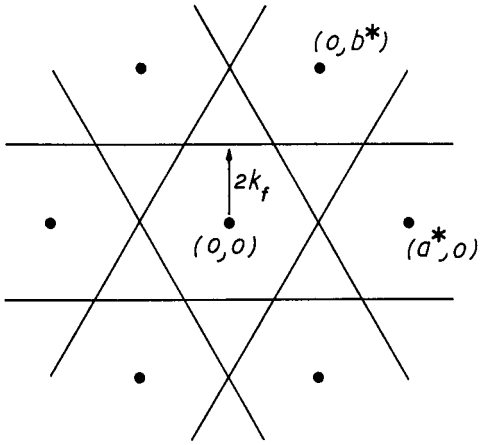

Figure 14. Schematic representation of the X-ray pattern in the (*a**, *b**)-plane above 120 K expected from the hidden nesting of KMo_6O_{17}. The heavy dots refer to Bragg reflections.

of Figure 14 condense into satellite reflections at *a**/2, *b**/2, and (*a** − *b**)/2, which are the cross-section points of the diffuse lines. The nesting in the real Fermi surfaces (Figures 13d) is not so complete as in the hidden surfaces (Figure 13e), so that some small pieces of the Fermi surface (for example, small electron and hole pockets) may remain (especially in the avoided crossing regions) after the CDW phase transition. This result would explain the semimetallic properties of AMo_6O_{17} observed below 120 K by galvanometric measurements.[14,36] Angle-resolved photoemission experiments on the sodium purple bronze also confirmed the occurrence of hidden nesting in these bronzes.[42,43]

The concept of hidden nesting was soon found essential in explaining the resistivity anomalies of a numer of oxides and bronzes such as the Magnéli phases γ- and η-Mo_4O_{11}[44] and the family of monophosphate tungsten bronzes $(PO_2)_4(WO_3)_p(WO_3)_q$ (*p* an *q* are integer numbers related to the width of the octahedral layers).[20] These solids also contain metal−oxygen layers made up of MO_6 octahedra and possess partially filled t_{2g}-block bands. As for the purple bronzes, the three t_{2g}-block orbitals of each MO_6 octahedron are contained in three mutually orthogonal planes, and act as δ-orbitals toward the M−O axes perpendicular to these planes. Consequently, as a first approximation, these metal−oxygen layers can be regarded as made up of three noninteracting sets of t_{2g}-orbital containing chains, as far as their t_{2g}-block bands are concerned. The interest of the Magnéli phases and the monophosphate tungsten bronzes is that the three t_{2g}-orbital containing chains are not equivalent.[19] This result leads to interesting new features in the low-temperature behavior of these solids that have recently received a lot of attention.[9d,9e,15−19]

This analysis also applies to other oxides and bronzes, such as the diphosphate tungsten bronzes[10] and the platinum bronzes,[45] and layered phases, such as $Sr_{n+1}V_nO_{3n+1}$[21,24] or the ternary nickelates $Ln_{n+1}Ni_nO_{3n+1}$.[46] The concept of hidden nesting was also found essential in explaining the electronic instabilities of structurally different systems; that is, the metal-to-insulator transitions of some organic conducting salts[24] and the CDW phenomena of the layered transition-metal dichalcogenides 1T-MX_2 (X = S, Se, Te).[47] Hidden nesting may also be relevant in understanding the

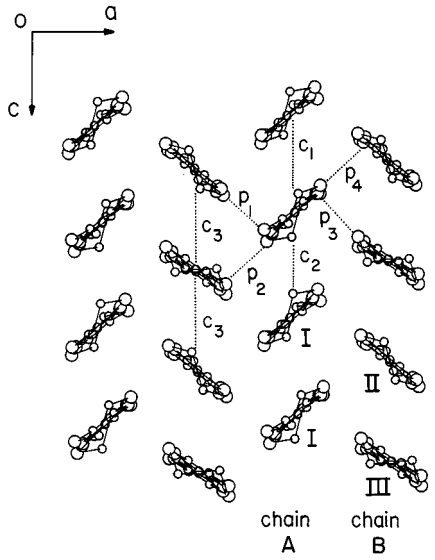

Figure 15. Perspective view of a BEDT-TTF layer of α-(BEDT-TTF)$_2$MHg(XCN)$_4$ where the different interactions are defined. Each molecule is viewed approximately along its central C=C bond, and the hydrogen atoms are not shown for simplicity.

origin of some surface reconstructions.[48] In general, the concept of hidden nesting should be applicable for the description of the electronic instabilities of many systems with several partially filled bands.

Understanding the Nature of the States at the Fermi Level: 1D versus 2D Character of the Charge Carriers in α-(BEDT-TTF)$_2$MHg(XCN)$_4$ (M = Tl, K, NH$_4$; X = S, Se) Molecular Metals

Let us now consider the question of the dimensionality of the charge carriers of the α-(BEDT-TTF)$_2$MHg(XCN)$_4$ (M = Tl, K, NH$_4$; X = S, Se) molecular metals.[49−52] These phases are 2D metals and have provided a seemingly endless series of intriguing results.[53−68] Their room-temperature crystal structures, as well as the band structures and Fermi surfaces calculated on the basis of such crystal structures, are very similar.[50,69,70] However, the low-temperature behavior is remarkably different. All of these salts exhibit Shubnikov−de Haas oscillations associated with closed 2D sections of the Fermi surface. At the same time, some of the salts of this family exhibit a low-temperature resistivity anomaly, which is believed to originate from a density wave instability due to the presence of nested 1D parts of the Fermi surface. Thus, despite being 2D metals, these salts must have two different types of charge carriers with different dimensionality. This conclusion is confirmed by several calculations of the Fermi surface.[50,69−71]

The members of the isostructural α-(BEDT-TTF)$_2$MHg(XCN)$_4$ family (M = Tl, K, NH$_4$; X = S, Se) contain layers of donor molecules BEDT-TTF that alternate with [MHg(XCN)$_4$] layers.[49−52] A perspective view of one BEDT-TTF layer is shown in Figure 15. The BEDT-TTF layer is constructed from two nonequivalent stacks parallel to the *c*-axis. One of them is formed by the cation-radicals I (the successive donors along the stack are related by inversion centers, i.e.,··I··I$_i$··I··), whereas the other contains the II and III ones (··III··II··III··). The stacks ··I··I$_i$··I·· and ··III··II··III·· pack side-by-side

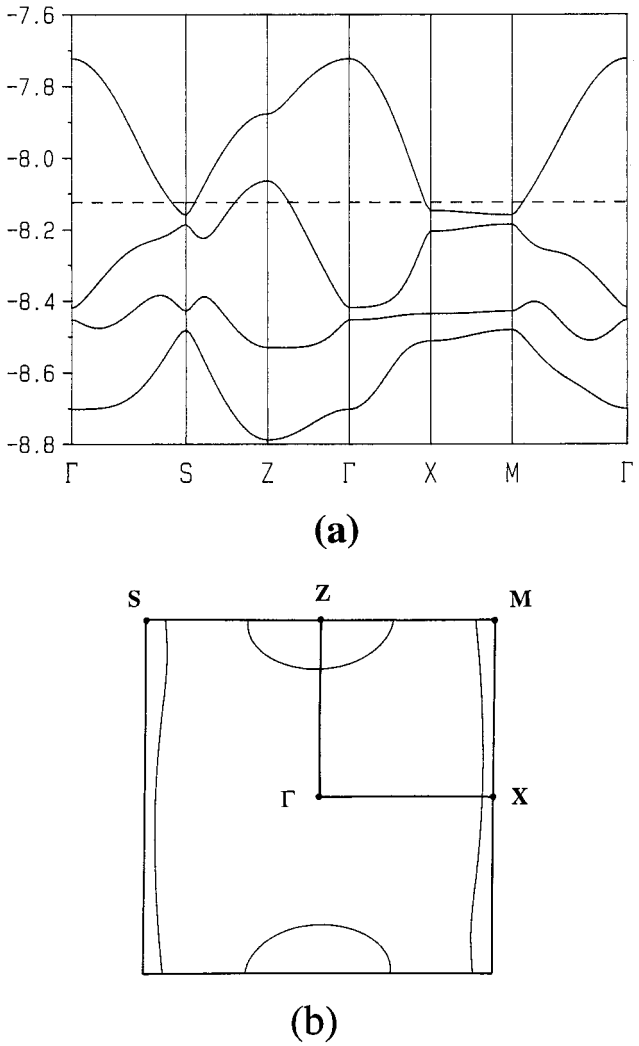

Figure 16. (a) Calculated band structure and (b) Fermi surface for the α-(BEDT-TTF)$_2$TlHg(SCN)$_4$ salt. In a the energies are given in eV and the dashed line indicates the Fermi level. Γ, X, Z, S, and M refer to the wave vectors (0, 0), (*a**/2, 0), (0, *c**/2), (-*a**/2, *c**/2), and (*a**/2, *c**/2), respectively.

along the *a*-axis. Within these donor layers there are many short S···S intermolecular contacts. Assuming the usual oxidation states of M^+, Hg^{2+}, and $(SCN)^-$, the average charge per BEDT-TTF donor molecule is +1/2. The nonintegral charge of the BEDT-TTF donors and the existence of short S···S contacts between the different donors of the layer are at the origin of the metallic conductivity of these salts.

The calculated band structure near the Fermi level for a representative example of these salts [i.e., α-(BEDT-TTF)$_2$TlHg(SCN)$_4$] is shown in Figure 16a. As expected, the four bands in Figure 16a are almost exclusively made of the HOMO of the four BEDT-TTF molecules of the unit cell. Hence, from now on we will refer to these four bands as the HOMO bands. With the average oxidation state of $(BEDT\text{-}TTF)^{+1/2}$ there are six electrons to fill these four bands. Because the third and fourth bands (from the bottom) overlap, the system should be metallic and the Fermi surface should exhibit both electron and hole contributions.

The calculated Fermi surface is shown in Figure 16b. The hole contribution (i.e., the part of the Fermi surface arising from the almost filled band) is closed whereas

Table 2. Transfer Integrals (eV) for the Different Donor···Donor Interactions Used in our Model Study [Integrals Were Calculated on the Basis of the 104 K Crystal Structure of α-(BEDT-TTF)$_2$KHg(SCN)$_4$]

interaction type[a]	transfer integral	interaction type[a]	transfer integral
c_1	−0.012	p_1	0.129
c_2	0.140	p_2	0.116
c_3	0.074	p_3	0.162
		p_4	0.161

[a] For labeling of the interactions see Figure 15.

the electron contribution (i.e., the part of the Fermi surface arising from the almost empty band) is open and parallel to the c*-direction. The results of Figure 16 are very similar to those for all other α-(BEDT-TTF)$_2$MHg(XCN)$_4$ salts whose crystal structures are presently known.[70] The results correctly describe the main aspects of the electronic structure of the these salts; that is, their metallic character and the existence of both 1D and 2D types of carriers.

At this point we must inquire why the Fermi surface of these salts possess both 1D and 2D portions. Is there actually a structural motif causing this; that is, is there actually a chain in the BEDT-TTF slabs? If yes, where are such chains and why is there a closed 2D orbit in the Fermi surface as well? Let us also remember that the open part of the Fermi surface is made of two warped lines along a direction perpendicular to the *a*-direction. Thus, if there are chains in the BEDT-TTF slabs, they should be along the *a*-direction. However, Figure 15 seems to suggest the existence of chains along the *c*-direction.

The more convenient way to tackle the problem is by using the well-known tight-binding equations for the energy versus *k* dependence as a function of the different transfer integrals of the lattice.[72] Only the HOMO of BEDT-TTF will be considered. The transfer integrals used in this model study were calculated from the 104 K crystal structure[50] of the α-(BEDT-TTF)$_2$KHg(SCN)$_4$ salt and are those reported in Table 2. These transfer integrals should provide the best approximation to the low temperature and ambient pressure Fermi surface. Calculations using transfer integrals calculated from the other crystal structures lead to the same results. The different transfer integrals are defined in Figure 15. Three of these transfer integrals (c_1 to c_3) will be referred to as intrachain transfer integrals and the remaining four (p_1 to p_4) as interchain transfer integrals. As discussed before, the donor lattice can be described as containing two different types of donor chains (A and B). Chain A contains only one type of donors (I, I_i) whereas chain B contains two different types (II and III).

Let us first consider the transfer integrals of Table 2. Of the c-type interaction energies only c_2 is sizable in chain A. Although from just a visual inspection this chain appears to be just that, a chain, in terms of the electronic structure it is a series of weakly interacting dimers. From now on we will call them c_2 dimers. Consider now Figure 15 in the light of this fact. It can be seen that the integrals p_2 and p_3 are different from their counterparts p_1 and p_4 in their orientation with respect to this dimer. In fact, we can see that the different c_2 dimers interact through donors III (interactions p_2 and p_3) to form a chain along the *a*-direction. Thus, at least conceptually, it is tempting to consider the lattice of the α-(BEDT-TTF)$_2$MHg(XCN)$_4$ phases as being made of chains of donors III and I (c_2 dimers) that communicate through donors II.

To further explore this idea, we carried out a series of model calculations where, taking the transfer integrals calculated for the 104 K structure of the α-(BEDT-TTF)$_2$KHg(SCN)$_4$ salt as the starting point, we gradually decreased the values of the p_1, p_4, and c_3 transfer integrals while keeping the other integrals constant. In such a way we gradually isolated the suggested chains within the lattice. The band structure of the lattice was calculated as a function of the parameter γ, which defines the different values of the p_1, p_4, and c_3 transfer integrals (t′) through the relationship $t' = \gamma t$, where t refers to the value in the 104 K crystal structure. The results are shown in Figure 17. For $\gamma = 1$ the band structure is very similar to the results of the full calculations (see Figure 16a for instance). For $\gamma = 0$ the band structure consists of a flat band, that of the noninteracting $HOMO_{II}$ levels (in the following, $HOMO_i$ (i = I, II, III) refers to the HOMO level of the type *i* BEDT-TTF), and a set of three bands characteristic of the chain along the *a*-direction. It is important to understand the topology of these three bands. Looking carefully at them it is easily seen that in fact they result from the interaction of a flat band (the second band at Γ) and two dispersive ones. When analyzing the orbital character of these bands it can be seen that the major components of the lower/upper dispersive bands are the bonding/antibonding combinations of the HOMOs of the c_2 dimer. The bonding/antibonding levels of the different c_2 dimers interact through the $HOMO_{III}$ and thus acquire dispersion (of course, leading to bands with opposite slope) along the Γ → X direction. Because the $HOMO_{III}$ levels are energetically between the bonding and antibonding HOMO levels of the c_2 dimer, they interact in a stabilizing way with the antibonding level but in a destabilizing way with the bonding one leading to a quite flat band.

Thus, the nature of the upper dispersive band and the completely flat one of Figure 17a ($\gamma = 0$) are easy to understand. It is these two bands that are going to lead to the two partially filled bands of the α-(BEDT-TTF)$_2$MHg(XCN)$_4$ phases. This result can be clearly seen in Figure 17. When we gradually switch the p_1, p_4, and c_3 interactions (i.e., γ changes from 0 to 1), the bands of the two subsystems mix. The originally flat band in the middle of the diagram mixes with all other bands and loses any trace of its original shape, leading to a band dispersive in any direction. The originally upper dispersive band is pushed up in energy but being the upper one, interacts essentially with the originally flat band and changes much less its shape. The important point, however, is that the shape is practically unaltered at the bottom of the band. Thus, there is a strong memory of the chain of c_2 dimers and donors III in the bottom of the upper band of the α-(BEDT-TTF)$_2$MHg(XCN)$_4$ phases. Thus, even though there is a 2D slab of donors in this system, the electrons at the bottom of the upper band experience significant 1D interactions and consequently contribute with 1D electron pockets to the Fermi surface.

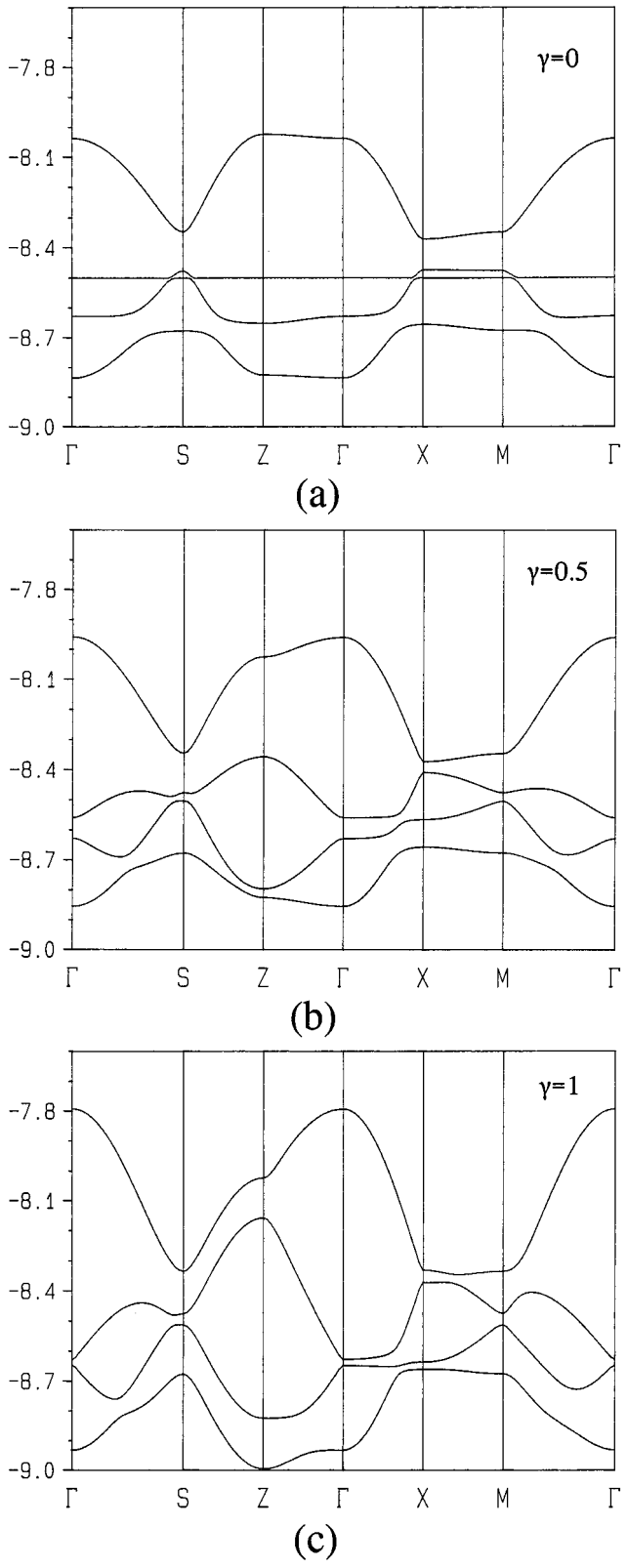

Figure 17. Model band structure for the α-(BEDT-TTF)$_2$MHg(XCN)$_4$ phases as a function of the parameter γ. The tight binding band structures were calculated on the basis of the transfer integrals evaluated for the 104 K structure of the α-(BEDT-TTF)$_2$KHg(SCN)$_4$ salt. The γ parameter defines the different actual values of the p_1, p_4, and c_3 transfer integrals (t′) used in the model calculations through the relationship $t' = \gamma t$, where t refers to the value in the 104 K crystal structure. All other transfer integrals were kept at their t values. Energies are given in eV.

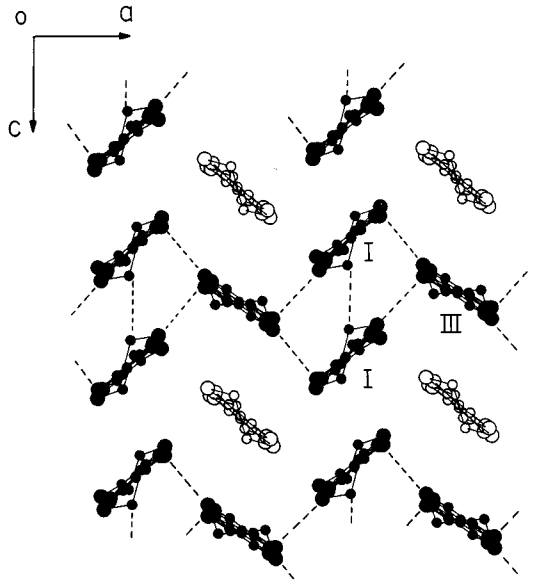

Figure 18. Schematic representation of the donor lattice of the α-(BEDT-TTF)$_2$MHg(XCN)$_4$ salts illustrating the nature of the "chains" leading to the 1D portion of the Fermi surface. The donors of the "chains" are shown with filled atoms and the "intrachain" interactions are marked with dotted lines.

As mentioned, the third band originates from the $HOMO_{II}$ levels, and its strong dispersion along all directions is caused by the switching of the p_1, p_4, and c_3 interactions. Hence, this band can be described as arising from the cross linking of the chains of the c_2 dimers and donors III through donors II. Therefore, the following physical model can be suggested to describe the electronic structure of the α-(BEDT-TTF)$_2$MHg(XCN)$_4$ phases. The electron pockets of the Fermi surface arise from the chains of c_2 dimers and donors III along the *a*-direction. The hole pockets of the Fermi surface originate from the coupling of such chains through donors II. Thus, the carriers of the Fermi surface of these phases see different aspects of the lattice. This model is schematically presented in Figure 18. With reference to this figure, the electron carriers only feel the interactions among the chains of donors in black, whereas the hole carriers feel all the interactions. At first sight this conclusion can appear quite strange. However, it is not. The reason lies again in the topology of the lattice. Because of the geometrical nature of the p_1 and p_4 interactions (i.e., those that are largely responsible for the coupling of the chains), their contributions can add or can compensate depending on the phase of the different HOMOs. In the second case the 1D character survives, but in the first one it completely disappears. The bottom of the fourth band lies in a region of the Brillouin zone where such phases impose a near cancellation of the p_1 and p_4 interactions whereas the opposite is true for the top of the third band. This result is why we can say that the electrons and holes of these phases see different aspects of the donor lattice.

This model, simple as it may be, makes it very easy to understand most of the results of previous theoretical studies on these phases and thus, it is probably a useful conceptual framework by which new experimental results can be rationalized. For instance, the 2D surface area was found to strongly depend on the p_1 and p_4

interactions.[70] This is because when the cross links between the chains increase, the system that the holes feel is more 2D and thus, the closed Fermi surface orbit becomes larger. The c_2 interaction was found to have the opposite effect.[70] It is clear from our discussion that the c_2 transfer integral controls the separation between the upper/lower bands of the chain (i.e., of the bands arising from the antibonding/bonding levels of the dimer). When c_2 increases, the separation between the bonding/antibonding levels of the dimer increases leading as a whole to a higher energy for the fourth band and thus, to a lower semimetallic overlap with the third band.

This model also explains the reported dependence of the Fermi surface area on the $HOMO_{II}$ energy.[70] As the $HOMO_{II}$ level is lower, which happens when the central C=C bond length is shorter, as in the α-(BEDT-TTF)$_2$MHg(XCN)$_4$ (M = Tl; X = Se, $Se_{0.875}S_{0.125}$; M = K; X = Se) salts, the initial nondispersive band (from which the third band originates) will also lie lower in energy and thus, the smaller will be the semimetallic overlap and the Fermi surface area. Thus, if the strength of the donor···donor interactions is not very different, as it has indeed shown to be the case, the area of the closed part of the Fermi surface of the α-(BEDT-TTF)$_2$MHg(XCN)$_4$ (M = Tl, X = Se, $Se_{0.875}S_{0.125}$; M = K, X = Se) salts calculated on the basis of their room-temperature crystal structures must be smaller than that calculated for the other α-(BEDT-TTF)$_2$MHg(XCN)$_4$ salts. This result was indeed found in detailed calculations.[70] According to the magnetoresistance experiments performed at very low temperatures, the reported area of the closed part of the Fermi surface for all the α-(BEDT-TTF)$_2$MHg(XCN)$_4$ salts is very similar, so thermal contraction must affect in a different way the crystal structure of the salts with similar or relatively different BEDT-TTF molecules in the donor layers.

It is not difficult to see how these ideas can be used to understand some experimental observations concerning these salts. It is clear from our proposed model (and we have verified this with model calculations) that the asymmetry of the 2D orbit with respect to the Z → M line of the Brillouin zone strongly depends on the relative value of the p_1 and p_4 interactions. As can be seen in Figures 15 and 18, the p_4 interaction acts in the ($a-c$)-direction whereas the p_1 interaction acts in the ($a+c$)-direction. If these two integrals are of different magnitude, the coupling between the chains in these two directions is different. This asymmetric coupling of the 1D chains can thus lead to such an asymmetry of the 2D hole Fermi surface if under the conditions of the measurement the difference between the p_1 and p_4 interactions is strong enough. For instance, such asymmetry has been reported for the K(S) salt.[73] Other experimental observations can also be simply understood on the basis of this model.

Concluding Remarks

The type of analysis reported here, although based on quite simple ideas of overlap, symmetry, and chemical bonding, provides a useful conceptual model by which the interesting physics and chemistry of many low-dimensional metals can be understood. More importantly, it also makes clear how carefully the dimensionality concept must be used. Quite frequently it is used in a purely structural sense. However, low-dimensional metals are interesting because of their peculiar transport properties. These properties, as well as the possible structural modulations exhibited by many of these systems, are determined by the topology of the Fermi surface. To understand them, we must be able to relate the Fermi surface and the crystal structure of the system, which means that we must consider just a small subset of the energy bands of the system (i.e., the partially filled ones). It is the dispersion of these partially filled bands what determines the shape of the Fermi surface and, consequently, the transport properties and the possible structural modulations. In contrast, from a purely orbital point of view, the structure of a system is determined by all the occupied energy levels (i.e., by the total energy of the system). Thus, there is no reason a solid with a given structural dimensionality could not exhibit transport and/or other physical properties indicating a lower dimensionality. Understanding the correlation between the crystal and the electronic structure is, and it will remain, an essential tool in the research on low-dimensional conductors.

Acknowledgment. The discussion reported stems very much from long-term collaborations with P. Batail (Nantes), J.-P. Pouget (Orsay), R.P. Shibaeva (Chernogolovka), and M.-H. Whangbo (Raleigh). I thank R. Rousseau for his significant contribution to the analysis of the electronic structure of molecular conductors. This work was partially supported by the DGES (Spain) Project PB96-0859 and Generalitat de Catalunya (1997 SGR 24).

References

(1) Peierls, R. In *Quantum Theory of Solids*; Oxford University: Oxford, 1955; p 108.
(2) Fröhlich, H. *Proc. Royal Soc. A* **1954**, *223*, 296.
(3) Wilson, J. A.; DiSalvo, F. J.; Mahajan, S. *Adv. Phys.* **1975**, *24*, 117.
(4) Williams, P. M. In *Crystallography and Crystal Chemistry of Materials with Layered Structures*; Lévy, F., Ed.; Reidel: Dordrecht, 1976; vol. 2, p 51.
(5) Ferraris, J.; Cowan, D. O.; Walatka, V. V.; Perlstein, J. H. *J. Am. Chem. Soc.* **1973**, *95*, 948.
(6) Coleman, L. B.; Cohen, M. J.; Sandman, D. J.; Yamagishi, F. G.; Garito, A. F.; Heeger, A. J., *Solid State Commun.* **1973**, *12*, 1125.
(7) Monceau, P.; Ong, N. P.; Portis, A. M.; Meerschaut, A.; Rouxel, J. *Phys. Rev. Lett.* **1976**, *37*, 602.
(8) Jérome, D.; Mazaud, A.; Ribault, M.; Bechgaard, K. *J. Physique Lett.* **1980**, *41*, L95.
(9) For representative reviews, see: (a) *Electronic Properties of Inorganic Quasi-One-Dimensional Compounds*; Monceau, P., Ed.; Reidel: Dordrecht, 1985; parts I and II; (b) *Crystal Chemistry and Properties of Materials with Quasi-One-Dimensional Structures*; Rouxel, J., Ed.; Reidel: Dordrecht, 1986; (c) *Structure Phase Transitions in Layered Transition Metal Compounds*; Motizuki, K.; Ed.; Reidel: Dordrecht, 1986; (d) *Low-Dimensional Electronic Properties of Molybdenum Bronzes and Oxides*; Schlenker, C., Ed.; Kluwer: Dordrecht, 1989; (e) *Physics and Chemistry of Low-Dimensional Inorganic Conductors*, NATO-ASI Series B: Physics; Greenblatt, M.; Schlenker, C.; Dumas, J.; van Smaalen, S., Eds.; Plenum: New York, 1996; (f) *Low Dimensional Conductors and Superconductors*, NATO-ASI Series B: Physics; Jérome, D.; Caron, L. G., Eds.; Plenum: New York, 1987; (g) Williams, J. M.; Ferraro, J. R.; Thorn, R. J.; Carlson, K. D.; Geiser, U.; Wang, H. H.; Kini, A. M.; Whangbo, M.-H. *Organic Superconductors*, Prentice Hall: New Jersey, 1992; (h) Ishiguro, T.; Yamaji, K. *Organic Superconductors*; Springer-Verlag: Berlin, 1990.
(10) Canadell, E.; Whangbo, M.-H. *Chem. Rev.* **1991**, *91*, 965.
(11) Ashcroft, N. W.; Mermin, N. D. *Solid State Physics*, Holt, Rinehart and Winston: Philadelphia, 1985.

(12) Mott, N. F. *Metal−Insulator Transitions*; Barnes and Noble: New York, 1977.
(13) (a) Greenblatt, M. *Chem. Rev.* **1988**, *88*, 31; (b) Schlenker, C.; Dumas, J.; Escribe-Filippini, C.; Guyot, H.; Marcus, J.; Fourcadot, J. *Philos. Mag. B* **1985**, *52*, 643.
(14) Dumas, J.; Schlenker, C. *Int. J. Mod. Phys. B* **1993**, *7*, 4045.
(15) Greenblatt, M. *Int. J. Mod. Phys. B* **1993**, *7*, 3937.
(16) (a) Foury, P.; Pouget, J. P. *Int. J. Mod. Phys. B* **1993**, *7*, 3973; (b) Ottolenghi, A.; Pouget, J. P. *J. Phys. I France* **1996**, *6*, 1059.
(17) Schlenker, C.; Hess, C.; Le Touze, C.; Dumas, J. *J. Phys. I France* **1996**, *6*, 2061.
(18) (a) Canadell, E.; Whangbo, M.-H. *Phys. Rev. B* **1991**, *43*, 1894; (b) Wang, E.; Greenblatt, M.; Rachidi, I. E.-I.; Canadell, E.; Whangbo, M.-H.; Vadlamannati, S. *Phys. Rev. B* **1989**, *39*, 12969.
(19) Canadell, E.; Whangbo, M.-H. *Int. J. Mod. Phys. B* **1993**, *7*, 4005.
(20) Raveau, B. *Proc. Indian Nat. Sci. Acad.* **1986**, *A52*, 67.
(21) Rousseau, R.; Palacín, M. R.; Gómez-Romero, P.; Canadell, E. *Inorg. Chem.* **1996**, *35*, 6396.
(22) Rousseau, R.; Canadell, E,; Alemany, P.; Galván, D. H.; Hoffmann, R. *Inorg. Chem.* **1997**, *36*, 4627.
(23) (a) Nozaki, A.; Yoshikawa, H.; Wada, T.; Yamauchi, H.; Tanaka, S., *Phys. Rev. B* **1991**, *43*, 181; (b) Suzuki, N.; Noritake, T.; Yamamoto, N.; Hiroki, T. *Mater. Res. Bull.* **1991**, *26*, 1.
(24) Whangbo, M.-H.; Ren, J.; Liang, W.; Canadell, E.; Pouget, J.-P.; Ravy, S.; Williams, J. M.; Beno, M. A. *Inorg. Chem.* **1992**, *31*, 4169.
(25) Adams, S.; Ehses, K.-H.; Spilker, J. *Acta Crystallogr. B* **1993**, *49*, 958.
(26) Onoda, M.; Toriumi, K.; Matsuda, Y.; Sato, M. *J. Solid State Chem.* **1987**, *66*, 163.
(27) (a) Schlenker, C.; Schwenk, H.; Escribe-Filippini, C.; Marcus, J. *Physica* **1985**, *135B*, 511; (b) Greenblatt, M.; McCarroll, W. H.; Neifeld, R.; Croft, M.; Waszczak, J. V. *Solid State Commun.* **1984**, *51*, 671.
(28) Smith, K. E.; Breuer, K.; Stagarescu, C.; Greenblatt, M.; McCarroll, W.; Ramanujachary, K. In *Physics and Chemistry of Low-Dimensional Inorganic Conductors*, NATO-ASI Series B: Physics; Greenblatt, M.; Schlenker, C.; Dumas, J.; van Smaalen, S., Eds.; Plenum: New York, 1996; p 313.
(29) Whangbo, M.-H.; Canadell, E. *J. Am. Chem. Soc.* **1988**, *110*, 358.
(30) (a) Batail, P.; Boubekeur, K.; Davidson, A.; Fourmigué, M.; Lenoir, C.; Livage, C.; Pénicaud, A. In *The Physics and Chemistry of Organic Superconductors*; Saito, G., Kagoshima, S., Eds.; Springer-Verlag: Berlin, 1990; p 353; (b) Davidson, A.; Boubekeur, K.; Pénicaud, A.; Auban, P.; Lenoir, C.; Batail, P.; Hervé, G. J. *J. Chem. Soc., Chem. Comm.* **1989**, 1373; (c) Pénicaud, A.; Batail, P.; Coulon, C.; Canadell, E.; Perrin, C. *Chem. Mater.* **1990**, *2*, 123; (d) Batail, P.; Ouahab, L.; Pénicaud, A.; Lenoir, C.; Perrin, A. *C. R. Acad. Sci. Paris Ser II* **1987**, *304*, 1111; (e) Boubekeur, K., Ph.D. Thesis, University of Rennes, France, 1989; (f) Pénicaud, A.; Lenoir, C.; Batail, P.; Coulon, C.; Perrin, A. *Synth. Met.* **1989**, *32*, 25; (g) Batail, P.; Livage, C.; Parkin, S. S. P.; Coulon, C.; Martin, J. D.; Canadell, E. *Angew. Chem., Int. Ed. Engl.* **1991**, *30*, 1498.
(31) For a recent review see: Coronado, E.; Gómez-García, C. *Chem. Rev.* **1998**, *98*, 273.
(32) Pénicaud, A.; Boubekeur, K.; Batail, P.; Canadell, E.; Auban-Senzier, P.; Jérome, D. *J. Am. Chem. Soc.* **1993**, *115*, 4101.
(33) Uriel, S.; Boubekeur, K.; Batail, P.; Orduna, J.; Canadell, E. *Inorg. Chem.* **1995**, *34*, 5307.
(34) Batail, P.; Boubekeur, K.; Guilbaud, C.; Pasquier, C.; Auban-Senzier, P.; Jérome, D.; Rousseau, R.; Canadell, E., unpublished results.
(35) Whangbo, M.-H.; Canadell, E.; Foury, P.; Pouget, J. P. *Science* **1991**, *252*, 96.
(36) Schlenker, C., Dumas, J., Escribe-Filippini, C.; Guyot, H. In *Low-Dimensional Electronic Properties of Molybdenum Bronzes and Oxides*; Schlenker, C., Ed.; Kluwer: Dordrecht, 1989; p 159.
(37) Greenblatt, M. In *Low-Dimensional Electronic Properties of Molybdenum Bronzes and Oxides*; Schlenker, C., Ed.; Kluwer: Dordrecht, 1989; p 1.
(38) Pouget, J. P. In *Low-Dimensional Electronic Properties of Molybdenum Bronzes and Oxides*; Schlenker, C., Ed.; Kluwer: Dordrecht, 1989; p 87.
(39) Vincent, H.; Ghedira, M.; Marcus, J.; Mercier, J.; Schlenker, C. *J. Solid State Chem.* **1987**, *47*, 113.
(40) Whangbo, M.-H.; Canadell, E.; Schlenker, C. *J. Am. Chem. Soc.* **1987**, *109*, 6308.
(41) Moret, R.; Pouget, J. P. in *Crystal Chemistry and Properties of Materials with Quasi-One-Dimensional Structures*; Rouxel, J., Ed.; Reidel: Dordrecht, 1986; p 87.
(42) Breuer, K.; Stagarescy, C.; Smith, K. E.; Greenblatt, M.; Ramanujachary, K. *Phys. Rev. Lett.* **1996**, *76*, 3172.
(43) Gweon, G.-H.; Allen, J. W.; Claessen, R.; Clack, J. A.; Poirier, D. M.; Benning, P. J.; Olson, G. C.; Ellis, W. P.; Zhang, Y.-X.; Schneemeyer, L. F.; Marcus, J.; Schlenker, C. *J. Phys.: Condens. Matter* **1996**, *8*, 9923.
(44) (a) Ghedira, M.; Vincent, H.; Marezio, M.; Marcus, J.; Fourcadot, G. *J. Solid State Chem.* **1985**, *56*, 66; (b) Kihlborg, L. *Arkiv Kemi* **1963**, *21*, 365; (c) Magnéli, A. *Acta Chem. Scand.* **1948**, *2*, 861.
(45) Doublet, M.-L.; Canadell, E.; Whangbo, M.-H. *J. Am. Chem. Soc.* **1994**, *116*, 2115.
(46) Seo, D.-K.; Liang, W.; Whangbo, M.-H.; Zhang, Z.; Greenblatt, M. *Inorg. Chem.* **1996**, *35*, 6396.
(47) Whangbo, M.-H.; Canadell, E. *J. Am. Chem. Soc.* **1992**, *114*, 9587.
(48) Burdett, J. K.; Canadell, E., *J. Chem. Phys.* **1995**, *103*, 6283.
(49) Oshima, M.; Mori, H.; Saito, G.; Oshima, K. *Chem. Lett.* **1989**, 1159.
(50) Mori, H.; Tanaka, S.; Oshima, M.; Saito, G.; Mori, T.; Maruyama, Y.; Inokuchi, H. *Bull. Chem. Soc. Jpn.* **1990**, *63*, 2183.
(51) Shibaeva, R. P.; Rozenberg, L. P. *Crystallogr. Rep.* **1994**, *39*, 47.
(52) Shibaeva, R. P.; Rozenberg, L. P.; Kushch, N. D.; Yagubskii, E. B. *Crystallogr. Rep.* **1994**, *39*, 747.
(53) Sasaki, T.; Toyota, N.; Tokumoto, M.; Kinoshita, N.; Anzai, H. *Solid State Comm.* **1990**, *75*, 93.
(54) Kinoshita, N.; Tokumoto, M.; Anzai, H. *J. Phys. Soc. Jpn.* **1991**, *60*, 2131.
(55) Kushch, N. D.; Buravov, L. V.; Kartsovnik, M. V.; Laukhin, V. N.; Pesotskii, S. I.; Shibaeva, R. P.; Rozenberg, L. P.; Yagubskii, E. B.; Zvarykina, A. V. *Synth. Met.* **1992**, *46*, 271.
(56) Kartsovnik, M. V.; Kovalev, A. E.; Kushch, N. D. *J. Phys. I France* **1993**, *3*, 1187.
(57) Wang, H.-H.; Carlson, K. D.; Geiser, U.; Kwok, W. K.; Vashon, M. D.; Thompson, J. E.; Larsen, N. F.; McCabe, G. D.; Hulscher, R. S.; Williams, J. M. *Physica C* **1990**, *166*, 57.
(58) Schegolev, A. I.; Laukhin, V. N.; Khomenko, A. G.; Kartsovnik, M. V.; Shibaeva, R. P.; Rozenberg, L. P.; Kovalev, A. E. *J. Phys. I France* **1992**, *2*, 2123.
(59) Buravov, L. V.; Kushch, N. D.; Laukhin, V. N.; Khomenko, A. G.; Yagubskii, E. B.; Kartsovnik, M. V.; Kovalev, A. E.; Rozenberg, L. P.; Shibaeva, R. P.; Tanatar, M. A.; Yefanov, V. S.; Dyakin, V. V.; Bondarenko, V. A. *J. Phys. I France* **1994**, *4*, 441.
(60) Brooks, J. S.; Agosta, C. C.; Klepper, S. J.; Tokumoto, M.; Kinoshita, N.; Anzai, H.; Uji, S.; Aoki, H.; Perel, A. S.; Athas, G. J.; Howe, D. A. *Phys. Rev. Lett.* **1992**, *69*, 156.
(61) Klepper, S. J.; Brooks, J. S.; Chen, X.; Bradaric, I.; Tokumoto, M.; Kinoshita, N.; Tanaka, Y.; Agosta, C. C. *Phys. Rev. B* **1993**, *48*, 9913.
(62) Osada, T.; Yagi, R.; Kagoshima, S.; Miura, N.; Oshima, M.; Saito, G. *Phys. Rev. B* **1990**, *41*, 5428.
(63) Pratt, F. L.; Singleton, J.; Doporto, M.; Fisher, A. J.; Janssen, T. J. B. M.; Perenboom, J. A. A. J.; Kurmoo, M.; Day, P. *Phys. Rev. B* **1992**, *45*, 13904.
(64) Wosnitza, J.; Crabtree, G. W.; Wang, H.-H.; Carlson, K. D.; Vashton, M. D.; Williams, J. M. *Phys. Rev. Lett.* **1991**, *67*, 263.
(65) Doporto, M.; Pratt, F. L.; Singleton, J.; Kurmoo, M.; Hayes, W. *Phys. Rev. Lett.* **1992**, *69*, 991.
(66) Sasaki, T.; Toyota, N. *Phys. Rev. B* **1994**, *49*, 10120.
(67) Kovalev, A. E.; Kartsovnik, M. V.; Kushch, N. D. *Solid State Commun.* **1993**, *87*, 705.
(68) Auban-Senzier, P.; Audouard, A.; Laukhin, V. N.; Rousseau, R.; Canadell, E.; Brossard, L.; Jérome, D.; Kushch, N. D. *J. Phys. I France* **1995**, *5*, 1301.
(69) Ducasse, L.; Fritsch, A. *Solid State. Comm.* **1994**, *91*, 201.
(70) Rousseau, R.; Doublet, M.-L.; Canadell, E.; Shibaeva, R. P.; Khasanov, S. S.; Rozenberg, L. P.; Kushch, N. D.; Yagubskii, E. B. *J. Phys. I* **1996**, *6*, 1527.
(71) Campos, C. S.; Sandhu, P. S.; Brooks, J. S.; Ziman, T. *Phys. Rev. B* **1996**, *53*, 12725.
(72) Grant, P. M. *J. Phys. Colloq. France* **1983**, *44*, C3−847.
(73) Kovalev, A. E.; Kartsovnik, M. V.; Shibaeva, R. P.; Rozenberg, L. P.; Schegolev, I. F.; Kushch, N. D. *Solid State Comm.* **1994**, *89*, 575.

CM980176O